Shadow-Aware Nonlinear Spectral Unmixing for Hyperspectral Imagery

Guichen Zhang, Paul Scheunders, *Senior Member, IEEE*, Daniele Cerra, *Member, IEEE*, and Rupert Müller

***Abstract*—In hyperspectral imagery, differences in ground surface structures cause a large variation in the optical scattering in sunlit and (partly) shadowed pixels. The complexity of the scene demands a general spectral mixture model that can adapt to the different scenarios of the ground surface. In this article, we propose a physics-based spectral mixture model, i.e., the extended shadow multilinear mixing (ESMLM) model that accounts for typical ground scenarios in the presence of shadows and nonlinear optical effects, by considering multiple illumination sources. Specifically, the diffuse solar illumination alters as the wavelength changes, requiring a wavelength-dependent modeling of shadows. Moreover, we allow different types of nonlinear interactions for different illumination conditions. The proposed model is described in a graph-based representation, which sums up all possible radiation paths initiated by the illumination sources. Physical assumptions are made to simplify the proposed model, resulting in material abundances and four physically interpretable parameters. Additionally, shadow-removed images can be reconstructed. The proposed model is compared with other state-of-the-art models using one synthetic dataset and two real datasets. Experimental results show that the ESMLM model performs robustly in various illumination conditions. In addition, the physically interpretable parameters contain valuable information on the scene structures and assist in performing shadow removal that outperforms other state-of-the-art works.**

***Index Terms*—Hyperspectral imagery, HySpex, nonlinear effect, nonlinear spectral unmixing, shadow-aware, spectral mixing models.**

I. Introduction

HYPERSPECTRAL cameras, also referred to as imaging spectrometers, record the spectral information of ground materials across many contiguous and narrow spectral channels and have become a valuable data source in remote sensing [1]–[3]. Each pixel in a spaceborne or airborne hyperspectral image captures the signal backscattered from a mixture of ground objects and atmospheric features [4]. In order to remove atmospheric features, atmospheric correction methods convert the signal to ground material reflectance [5]–[7]. As a pixel typically contains more than one material, the spectrum of a pixel at reflectance level is given as a mixture of the spectral signatures of the materials (i.e., endmembers) contained in a single-resolution cell. Spectral unmixing reveals the endmembers and their corresponding contributions (i.e., abundances) [8]–[10]. Developing a good mixture model is one of the uttermost important prior conditions for a successful spectral unmixing process.

Methods based on radiative transfer [11], [12] model the optical interactions of the entire imaging chain and can build an accurate mixture model. However, they often require detailed geometric and radiometric auxiliary data. Additionally, due to their complexity, inversing these models is nontrivial [9]. Thus, in the past decades, many researchers have derived simplified physics-based mixture models following various assumptions. The most common model, the linear mixing model (LMM) [13], follows the straightforward assumption that the incoming solar illumination interacts with a pixel only once before being scattered back to the sensor. The spectral mixture is then given by the sum of the material spectra, weighted by their spatial proportion within the pixel. This simple model assumes an ideal scene structure, with a flat ground surface and spatially separable ground materials [9], [10]. Two constraints on the abundances are often applied along with the LMM [8]. As abundances are areal proportion values per pixel, they are constrained to positive values (ANC, abundance nonnegativity constraint). Assuming that the endmember library includes all possible materials in a scene, the sum of abundance values per pixel equals one (ASC, abundance sum-to-one constraint). Some later works relax the ASC constraint, allowing some materials in a pixel not to be present in the endmember library [8]. In addition, other constraints on the abundances have been also applied along with the LMM, such as sparsity [14]–[16] and spatial constraints [17], [18].

The linear mixture model depends on strict physical assumptions that are often not fulfilled in reality. In many situations, nonlinear optical interactions are nonnegligible [9], [10], [19]. Nonlinear mixtures can occur at both microscopic and macroscopic levels [10] and, depending on the size of the particles under investigation, different categories of models exist. At the microscopic level, intimate mixtures occur, in which the optical interactions with grains or particles are typically smaller than the path length followed by the photons [10]. The most popular model is the Hapke model [20] that derives the measured reflectance as a function of optical and physical parameters of the medium. Intimate mixtures are not the focus of this article. In the macroscopic scenario, nonlinear optical interactions can occur because of height differences between ground objects [9],

Manuscript received 31 March 2022; revised 20 May 2022 and 20 June 2022; accepted 27 June 2022. Date of publication 6 July 2022; date of current version 20 July 2022. *(Corresponding author: Guichen Zhang.)*

Guichen Zhang, Daniele Cerra, and Rupert Müller are with the Remote Sensing Technology Institute (IMF), German Aerospace Center DLR, 82234 Weßling, Germany (e-mail: guichen.zhang@dlr.de; daniele.cerra@dlr.de; rupert.mueller@dlr.de).

Paul Scheunders is with the Imec-Vision Lab, Department of Physics, University of Antwerp, 2000 Wilrijk, Belgium (e-mail: paul.scheunders@uantwerpen.be).

Digital Object Identifier 10.1109/JSTARS.2022.3188896

[10]. In order to allow incoming light to interact more than once before being scattered back to the sensor, some nonlinear models use higher-order terms through the termwise product of spectra. Most methods only consider bilinear terms up to the second order. The parameters and constraints corresponding to the bilinear terms can follow different assumptions, leading to different nonlinear mixture models, such as the Nascimento model [21], the Fan model [22], the postnonlinear mixing model (PPNM) [23], and the generalized bilinear model (GBM) [24]. Meganem *et al.* [25] proposed a linear–quadratic model based on radiative transfer theory. This model has a similar form as the GBM [24], but it is entirely derived from physical equations with clear interpretations of the parameters.

Apart from bilinear models, some works have attempted to consider all orders of interactions using harmonic functions [26] and polynomial functions [27]. Recently, a multilinear mixing (MLM) model [28] has been proposed, based on the stochastic process of optical interactions with clear physical assumptions. This model traces the path that a single light ray follows and extends the optical interactions to infinite order, following physical assumptions. Besides abundances, this model includes one additional parameter P, which is the probability of a light ray undergoing further optical interactions after each previous interaction with ground materials. It is worth noting that this model follows the rule of conservation of energy: when $P > 0$, the reconstructed pixel does not increase its value with respect to the LMM result for the same endmembers and abundances. However, when a pixel receives additional illumination from its neighborhood, the observed spectrum can be larger than the reconstructed result by the LMM. This phenomenon can be achieved numerically by setting $P < 0$, with P losing its physical meaning.

Later, the MLM model has been extended to tackle shadow effects (the SMLM model) by including another parameter Q, representing the pixelwise fractional value of cast shadow [29]. The way of treating shadow in this work is equivalent to adding a "zero-reflectance" spectrum to the endmember library, which has been recognized as a straightforward manner to deal with shadows in spectral mixture models [30], [31]. This method assumes shadow to be an endmember and regards the shadow problem as a wavelength-independent scaling effect. Despite being able to model shadowed pixels with comparatively low reconstruction errors, this technique lacks physical interpretation, as the shadow endmember is not the spectrum of any ground material.

When treating shadow as a scaling effect, the spectral angle between sunlit and shadowed ground materials remains zero. Therefore, some methods apply spectral angle matching to pair sunlit and shadowed pixels containing the same material [32]–[35]. However, shadow not only scales a spectrum but also causes wavelength-dependent distortions [36]. Some works have paid attention to the spectral distortions caused by shadow. In an early work, a constant illumination is assumed and shadow is treated as a nonlinear effect [21]. The authors studied a specific situation, where trees block the direct solar illumination on a region covered by grass. Assuming that shadowed areas receive secondary illumination, the proposed method models the shadowed spectrum by the termwise product of the tree and grass spectra. Another group of methods allows the illumination conditions to vary over a scene. As shadowed pixels receive no or only a part of direct solar illumination, diffuse solar illumination is a prominent illumination source for shadowed pixels [37]. Yamazaki *et al.* [36] performed a field experiment to study the spectral characteristics of shadowed regions and showed that the shadow effect is strongly wavelength-dependent. Several more generic methods describe the shadow effects by introducing multiple illumination sources and applying the concept of spectral unmixing. Inspired by radiative transfer theory [37], Uezato *et al.* [38] developed a spectral unmixing method using hyperspectral data at a radiance level, coupled with a digital surface model. Zhang *et al.* [39] have presented a spectral mixture model based on reflectance data and have derived abundance values along with topographical information. Although it was shown that embedding multiple illumination sources in a model improves unmixing performances in (partly) shadowed pixels, nonlinearity has been modeled similarly for all pixels, regardless of the illumination conditions [39]. However, the nonlinearity in shadowed areas can behave quite differently from sunlit areas, due to the light attenuation caused by occluding objects.

In this article, we present a novel nonlinear mixture model, which is an extension of the SMLM model [29] and that overcomes the mentioned problems in the following aspects.

1) We consider two illumination sources, i.e., 1) direct and 2) diffuse solar illuminations. Following physical assumptions, we allow variable illumination conditions over the scene, where sunlit regions receive direct as well as diffuse solar illuminations, whereas shadowed regions receive diffuse solar illumination and possibly reflected direct solar illumination. Specifically, one pixel can be composed of shadowed areas along with fully sunlit areas and can, therefore, be treated as a partly shadowed pixel, resulting in a better representation of shadow boundaries.
2) Our proposed model allows two different types of nonlinear interactions. Besides the nonlinear optical interactions caused by the direct incoming light from both illumination sources, a pixel can receive secondary reflections from its neighboring pixels. In this way, the proposed model can produce reconstructed pixels with spectral values larger than those obtained through LMM, without losing the physical meaning of the parameter P, while energy conservation still holds.
3) We describe our model using a graphical representation with multiple illumination sources. The mixture result is computed as the sum of all light contributions, weighted by their probabilities. In addition to the abundances values, our model generates four pixelwise physically interpretable parameters: Q (spatial fraction of shadow in a pixel), F (sky view factor, which denotes the fraction of the sky hemisphere that is visible from the ground surface [40]), P (the probability of higher-order interactions of the incoming light ray), and K (a strength factor of neighbor interactions, denoting the fraction of the scattered light from the neighborhood that is received by the pixel).

TABLE I
NOTATIONS

Symbol	Description
λ	wavelength
L_p	path radiance
E_l	direct solar irradiance at ground surface
E_s	diffuse solar irradiance at ground surface
τ_{dir}	transmittance of the direct solar radiation
τ_{diff}	transmittance of the diffuse solar radiation
δ	direct solar irradiance indicator
L	at-sensor radiance with $\delta = 1$
L'	at-sensor radiance with $\delta = 0$
r	material reflectance
$\hat{r}$	estimated r by the atmospheric correction with $\delta = 1$
$\hat{r}_s$	estimated r by the atmospheric correction with $\delta = 0$
F	sky view factor
k_1,k_2,k_3	parameters describing the diffuse-to-direct solar irradiance
$\boldsymbol{x}$	observed pixel
$\boldsymbol{e}_i$	the $i-$th endmember
d	number of spectral bands
p	number of endmembers
N	number of pixels
path	a light path defined by the random variable $\{X_i\}_{i\geq 0} \in S$
P(path)	probability of path
L	light path length
S	a discrete set containing all possible interactions that a light ray can undergo from the illumination source(s) to the observer
$T(s_i)$	operator that acts on the light ray in state s_i
a_i	abundance of the endmember $\boldsymbol{e}_i$
$\gamma_{i,j}$	free parameter in bilinear mixing models corresponding to $\boldsymbol{e}_i$ and $\boldsymbol{e}_j$
P	the probability that a light ray undergoes additional interactions with endmembers
Q	spatial fraction of shadow
K	a strength factor of neighbor interactions, denoting the fraction of the scattered light from the neighborhood that is received by the pixel
$\boldsymbol{e}_N(i,j)$	the neighborhood spectrum of target pixel $\boldsymbol{x}(i,j)$
D	Euclidean distance between two pixels in the spatial domain
W	weight factor according to inverse distance between neighboring and target pixels
RE	mean reconstruction error
SRE	spectral reconstruction error
AE	mean abundance error

The remainder of this article is organized as follows. In Section II, we describe the impact of shadow on the observed reflectance, based on radiative transfer and atmospheric correction. Section III introduces the physics-based mixture models from the literature, whereas Section IV describes our proposed mixture model. Section V introduces the experimental setup, including three datasets for the evaluation of the spectral mixing models, quantitative measures for the comparison of the methods, the unmixing procedure, and the experimental design. Section VI demonstrates the experimental results quantitatively using a synthetic dataset, and Section VII and VIII present both quantitative and qualitative results using real datasets. Finally, we conclude our work and give future prospects in Section IX.

II. Impact of Shadow on Reflectance

A. Notations

Table I presents the notations used in this paper.

B. Impact of Shadow on Reflectance

A single-element detector of a spectrometer receives the backscattered solar radiation of a ground pixel, determined by the instantaneous field of view (IFOV) from different radiation paths. The backscattered radiation contains two contributions: 1) the radiation, scattered by the atmosphere to the single-element detector without interacting with the ground surface (path radiance); 2) the radiation interacting with the ground surface and scattered back to the single detecting element (reflected radiation). Following the theory of radiation propagation [7], [37], the incoming solar radiation reaching the ground surface mainly consists of two portions. The most significant portion is the "direct solar irradiance (direct sunlight)," i.e., the direct solar illumination propagating through the atmosphere and reaching the ground surface. The remaining portion is the "diffuse solar irradiance (skylight)," i.e., the solar radiation dispersed in the atmosphere before reaching the ground surface. The contribution of skylight as an illumination source is significantly smaller with respect to direct sunlight, but it is nonnegligible in some situations, such as overcast sky and shadowed areas [37].

Let us assume that the ground targets are located on a flat terrain and behave as a Lambertian surface. Then, at each wavelength λ, the at-sensor radiance $L(\lambda)$ for a ground pixel with reflectance $r(\lambda)$ can be written as

$$L(\lambda) = L_p(\lambda) + \frac{\delta \tau_{\text{dir}}(\lambda) E_l(\lambda) r(\lambda)}{\pi} + \frac{\tau_{\text{diff}}(\lambda) E_s(\lambda) r(\lambda)}{\pi} \tag{1}$$

where $L_p(\lambda)$ is the path radiance, $E_l(\lambda)$ the direct solar irradiance, and $E_s(\lambda)$ the diffuse solar irradiance on the ground target. The transmittances of the direct and diffuse solar radiation are $\tau_{\text{dir}}(\lambda)$ and $\tau_{\text{diff}}(\lambda)$, respectively, while δ is a binary value indicating if the ground surface receives any direct solar irradiance. In traditional atmospheric correction algorithms, δ is set to 1, as the ground surface is usually assumed to be horizontal and unobstructed, i.e., it "sees" the entire hemisphere above. Thus, given the at-sensor radiance L, atmospheric correction is applied and $\hat{r}(\lambda)$ is derived by inverting (1)

$$\hat{r}(\lambda) = \frac{\pi(L(\lambda) - L_p(\lambda))}{\tau_{\text{dir}}(\lambda) E_l(\lambda) + \tau_{\text{diff}}(\lambda) E_s(\lambda)} = r(\lambda). \tag{2}$$

However, a pixel may not or only partly receive direct sunlight, due to occlusion by ground objects. The at-sensor radiance $L'(\lambda)$ of a fully shadowed pixel, containing one material with reflectance $r(\lambda)$, is given by (1) with $\delta = 0$

$$L'(\lambda) = L_p(\lambda) + \frac{\tau_{\text{diff}}(\lambda) E_s(\lambda) r(\lambda)}{\pi}. \tag{3}$$

When standard atmospheric correction (2) is applied on such a pixel, then the reflectance $\hat{r}_s(\lambda)$ is computed as

$$\hat{r}_s(\lambda) = \frac{\pi(L'(\lambda) - L_p(\lambda))}{\tau_{\text{dir}}(\lambda) E_l(\lambda) + \tau_{\text{diff}}(\lambda) E_s(\lambda)} = \frac{\tau_{\text{diff}}(\lambda) E_s(\lambda) r(\lambda)}{\tau_{\text{dir}}(\lambda) E_l(\lambda) + \tau_{\text{diff}}(\lambda) E_s(\lambda)} \tag{4}$$

in which (3) is substituted.

As reflectance represents an intrinsic property of a material and should not change according to illumination conditions, we expect that $\hat{r}_s(\lambda) = \hat{r}(\lambda) = r(\lambda)$. However, during atmospheric correction, the direct solar irradiance is incorrectly assumed to be an illumination source in shadowed regions. As a consequence,

the computed reflectance values in these areas are much smaller than their correct values, and a wavelength-dependent deviation exists between $\hat{r}_s(\lambda)$ and $r(\lambda)$.

If no occlusion occurs on a ground pixel, the diffuse radiation comes from all directions of the sky dome. Otherwise, the diffuse irradiance decreases by the sky view factor $F \in [0, 1]$, representing the fraction of sky that a ground pixel can "see." Following previous works, we model the decrease of the diffuse-to-direct solar irradiance as the wavelength goes up through a power function, which describes stronger atmospheric scattering at short wavelengths [37], [39], [41], [42]

$$\frac{\tau_{\text{diff}}(\lambda)E_s(\lambda)}{\tau_{\text{dir}}(\lambda)E_l(\lambda)} = F\left(k_1\lambda^{-k_2} + k_3\right) \tag{5}$$

with k_1, k_2, $k_3 > 0$.

Combining (4) and (5), we derived an expression for the reflectance of a ground material in fully shadowed regions with respect to the reflectance of the same material exposed to direct sunlight as

$$\hat{r}_s(\lambda) = \frac{F\left(k_1\lambda^{-k_2} + k_3\right)}{1 + F\left(k_1\lambda^{-k_2} + k_3\right)}\hat{r}(\lambda). \tag{6}$$

The derived relationship between the reflectances of the same material in different illumination conditions is only valid in the following simplified scenario. First, each ground pixel contains only one material. Second, illumination interacts only once with a ground pixel before being scattered back to the sensor. Third, a ground pixel can only be either fully sunlit or fully shadowed. In reality, a ground pixel can be composed of multiple materials, and illumination sources can interact multiple times with ground materials. In addition, pixels may only be partly shadowed. To include these situations, a shadow-aware nonlinear spectral mixture model is required.

III. Mixture Models and Their Graph Representations

The mixture models describe the optical interactions to a certain degree of complexity in the imaging chain [9], [10]. Following the work in [28] and [29], we present state-of-the-art spectral mixture models, based on a ray-based approximation of light and a graph-based representation of the optical interactions. We notate an observed pixel as a d-dimensional vector $\boldsymbol{x}$ and p endmember spectra as p d-dimensional vectors $\{\boldsymbol{e}_i\}_{i=1}^{p}$, where d denotes the number of spectral bands.

The entire process of the incoming light from the illumination sources undergoing optical interactions, and each sensitive element of the spectrometer recording the backscattered light from the corresponding ground pixel can be described as a discrete-time stochastic process [29]. A light path is defined by the random variable $\{X_n\}_{n\geq 0}$ with $\forall n\ X_n \in S$, and the discrete set S contains all possible interactions that a light ray can undergo before reaching the observer. In passive optical imaging, the light path always starts from the illumination source $X_0 = s_0$. States in which the light ray interacts with a ground material are indicated as $\{X_i = s_i\}_{i=1}^{L}$. Since we consider only the scattered light eventually received by the observer, a light path ends with the observer state $X_{L+1} = o$. $L \in [1, \infty]$ is the path length, indicating the number of optical interactions that a light ray underwent before being scattered back to the observer.

The probability of observing a certain path of length L is given by

$$P(\text{path}) = P(X_0 = s_0, X_1 = s_1, \ldots, X_L = s_L, X_{L+1} = o). \tag{7}$$

It is assumed that this stochastic process follows the Markov property:

$$P(X_{n+1}|X_0, \cdots X_n) = P(X_{n+1}|X_n). \tag{8}$$

At each state, the optical properties of the light ray will be altered. This alteration describes a relative change in the spectrum of the light ray, according to the reflectance of the object associated with that state. If $T(s_i)$ is the operator that acts on the light ray in state s_i, the total effect of path $= \{X_0 = s_0, X_1 = s_1, \ldots, X_L = s_L, X_{L+1} = o\}$ on a light ray is given by $\prod_{i=0}^{L} T(s_i)$. The operator $T(s_i)$ is associated with the state s_i.

1) For states $\{X_i = s_i\}_{i=1}^{L}$ representing ground materials, $T(s_i) = \boldsymbol{e}_i$.
2) For the state $\{X_{L+1} = o\}$ presenting the observer, $T(o) = \mathbf{1}$.
3) For the state $\{X_0 = s_0\}$ representing the illumination source(s), $T(s_0)$ is a constant vector and corresponds to the illumination source.

Thus, an observed pixel $\boldsymbol{x}$ is described as the weighted average over all possible paths

$$\boldsymbol{x} = \sum_{L=1}^{\infty}\left(\sum_{s_0\in S}\sum_{s_1\in S}\cdots\sum_{s_L\in S}\right)P(\text{path})\prod_{k=0}^{L}T(s_k). \tag{9}$$

Table II shows a summary of light paths, their corresponding probabilities, and spectral contributions for different mixing models. In the next sections, we will describe in more detail these models and their graph representations.

A. Linear Mixing Model

The linear mixing model (LMM) assumes that the incoming light interacts only once with a set of endmembers before being scattered back to the sensor ($L = 1$). The probability of an incoming light ray from the illumination source s that interacts with the ground surface with endmember $\boldsymbol{e}_l$, $(l = 1, \ldots, p)$ and is scattered back to the observer o is proportional to the abundance a_l, $(l = 1, \ldots, p)$. Thus: $P(\text{path}) = P(X_0 = s_0, X_1 = s_1, X_2 = o) = a_l$, and $\prod_{k=0}^{L} T(s_k) = T(s_0)T(s_1)$, with $T(s_0) = \mathbf{1}$ and $T(s_1) = \boldsymbol{e}_l$. According to (9), the LMM is written as

$$\boldsymbol{x} = \sum_{s_0\in S}\sum_{s_1\in S} a_l T(s_0)T(s_1) = \sum_{i=1}^{p} a_i\boldsymbol{e}_i \tag{10}$$

where $\sum_{i=1}^{p} a_i = 1$ and $\forall i$: $a_i \geq 0$.

B. Bilinear Mixing Models

In bilinear models, a light ray from the illumination source can either interact with an endmember once before being scattered

TABLE II
PROBABILITIES OF LIGHT PATHS AND THEIR SPECTRAL CONTRIBUTIONS IN DIFFERENT MIXING MODELS

Path	Probability	Contribution	Parameters	Model
$s_0 - \boldsymbol{e}_i - o$	a_i	$\boldsymbol{e}_i$	/	LMM [13]
$s_0 - \boldsymbol{e}_i - o$	a_i	$\boldsymbol{e}_i$	$\gamma_{i,j} = 0, if\ i \geq j$ $\gamma_{i,j} = 1, if\ i < j$	Fan [22]
$s_0 - \boldsymbol{e}_i - \boldsymbol{e}_j - o$	$\gamma_{i,j} a_i a_j$	$\boldsymbol{e}_i \odot \boldsymbol{e}_j$	$\gamma_{i,j} = b$	PPNM [23]
			$\gamma_{i,j} = 0,\ if\ i \geq j$ $\gamma_{i,j} \in [0,1], if\ i < j$	GBM [24]
$s_0 - \boldsymbol{e}_i - o$	$a_i(1-P)$	$\boldsymbol{e}_i$		
$s_0 - \boldsymbol{e}_i - \boldsymbol{e}_j - o$	$a_i a_j (1-P)P$	$\boldsymbol{e}_i \odot \boldsymbol{e}_j$		
$s_0 - \boldsymbol{e}_i - \boldsymbol{e}_j - \boldsymbol{e}_k - o$	$a_i a_j a_k (1-P)PP$	$\boldsymbol{e}_i \odot \boldsymbol{e}_j \odot \boldsymbol{e}_k$	$P \in [0,1]$	MLM [28]
$\cdots$	$\cdots$	$\cdots$		
$s_0 - \boldsymbol{e}_i - \boldsymbol{e}_j - \boldsymbol{e}_k \cdots \boldsymbol{e}_R - o$	$a_i a_j a_k \cdots a_R (1-P)P^{R-1}$	$\boldsymbol{e}_i \cdot \boldsymbol{e}_j \odot \boldsymbol{e}_k \cdots \boldsymbol{e}_R$		
$s_0 - \boldsymbol{e}_i - o$	$(1-Q)a_i$	$\boldsymbol{e}_i$	/	SLMM [28]
$s_0 - \boldsymbol{e}_i - o$	$(1-Q)a_i(1-P)$	$\boldsymbol{e}_i$		
$s_0 - \boldsymbol{e}_i - \boldsymbol{e}_j - o$	$a_i a_j (1-P)P$	$\boldsymbol{e}_i \odot \boldsymbol{e}_j$		
$s_0 - \boldsymbol{e}_i - \boldsymbol{e}_j - \boldsymbol{e}_k - o$	$a_i a_j a_k (1-P)PP$	$\boldsymbol{e}_i \odot \boldsymbol{e}_j \odot \boldsymbol{e}_k$	$P, Q \in [0,1]$	SMLM [29]
$\cdots$	$\cdots$	$\cdots$		
$s_0 - \boldsymbol{e}_i - \boldsymbol{e}_j - \boldsymbol{e}_k \cdots \boldsymbol{e}_R - o$	$a_i a_j a_k \cdots a_R (1-P)P^{R-1}$	$\boldsymbol{e}_i \odot \boldsymbol{e}_j \odot \boldsymbol{e}_k \cdots \boldsymbol{e}_R$		
$s_{0_{glob}} - \boldsymbol{e}_i - o$	$(1-Q)a_i$	$\boldsymbol{e}_i$		
$s_{0_{glob}} - \boldsymbol{e}_i - \boldsymbol{e}_j - o$	$a_i a_j$	$\boldsymbol{e}_i \odot \boldsymbol{e}_j$	/	Fansky [39]
$s_{0_{diff}} - \boldsymbol{e}_i - o$	Qa_i	$\boldsymbol{e}'_i$		

back the sensor, i.e., $L = 1$, or it can have multiple interactions with endmembers up to the second order, i.e., $L = 2$. Thus, we have two possible light paths, with probabilities: $P(\text{path}) = P(X_0 = s_0, X_1 = s_1, X_2 = o) = a_l$ and $P(\text{path}) = P(X_0 = s_0, X_1 = s_1, X_2 = s_2, X_3 = o) = \gamma_{m,n} a_m a_n$. Different bilinear models can be derived by constraining the free parameter $\gamma_{m,n}$ (see Table II). Then

$$\begin{aligned}\boldsymbol{x} = & \sum_{s_0 \in S} \sum_{s_1 \in S} a_l T(s_0) T(s_1) \\ & + \sum_{s_0 \in S} \sum_{s_1 \in S} \sum_{s_2 \in S} \gamma_{m,n} a_m a_n T(s_0) T(s_1) T(s_2) \\ = & \sum_{i=1}^{p} a_i \boldsymbol{e}_i + \sum_i \sum_j \gamma_{i,j} a_i a_j \boldsymbol{e}_i \odot \boldsymbol{e}_j. \end{aligned} \tag{11}$$

C. MLM Model

Recently, Heylen and Scheunders[28] extended bilinear mixing models to the MLM model that regards all orders of optical interactions. Similar to the case of linear and bilinear models, this assumes that a light ray incoming from the illumination source will interact with at least one material. Besides, the MLM model introduces a new parameter P: After each interaction with a material, the light ray will have a probability P of undergoing further interactions and a probability $(1 - P)$ of escaping the scene and reaching the observer. Following these assumptions, a light ray from the illumination source can interact with ground objects up to an infinite amount of times before being scattered back to the sensor, i.e., $L \in [1, \infty]$. Given a light path: path $= \{X_0 = s_0, X_1 = s_1, X_2 = s_2, \ldots, X_L = s_L, X_{L+1} = o\}$, its probability is given by $P(\text{path}) = (1-P)P^{L-1} a_{i_1} a_{i_2} \cdots a_{i_L}$. The spectral contribution of this path is $\prod_{k=0}^{L} \boldsymbol{e}_{i_k}$ with $\boldsymbol{e}_{i_k}$ representing the endmember of the material that the ray interacts with the k_{th} time and a_{i_k} its abundance.

Thus

$$\begin{aligned}\boldsymbol{x} &= \sum_{L=1}^{\infty} \left(\sum_{i_1=1}^{p} \cdots \sum_{i_L=1}^{p} \right) (1-P) P^{L-1} \prod_{k=1}^{L} (a_{i_k} \boldsymbol{e}_{i_k}) \\ &= (1-P) \sum_{i=1}^{p} a_i \boldsymbol{e}_i + (1-P)P \sum_{i=1}^{p} \sum_{j=1}^{p} a_i a_j \boldsymbol{e}_i \odot \boldsymbol{e}_j + \cdots \\ &= \frac{(1-P) \sum_{i=1}^{p} a_i \boldsymbol{e}_i}{1 - P \sum_{i=1}^{p} a_i \boldsymbol{e}_i}. \end{aligned} \tag{12}$$

D. Shadow LMM Model

The shadow LMM (SLMM) extends the endmember library with a "zero-reflectance" spectrum. Numerically, this technique is equivalent to including a parameter $Q \in [0, 1]$, which represents the spatial fraction of shadow in a pixel [28]. Values of $Q = 0$ and $Q = 1$ indicate a fully sunlit and fully shadowed pixel, respectively, while $Q \in (0, 1)$ describes a partly shadowed pixel. This model can estimate abundances under the shadow by setting $Q = 0$ during pixel reconstruction. Similar to the LMM, the light path of the SLMM is $P(s_0, \boldsymbol{e_l}, o) = (1-Q)a_l$ with the spectral contribution of $\boldsymbol{e}_l$. Thus

$$\boldsymbol{x} = \sum_{s_0 \in S} \sum_{s_1 \in S} (1-Q) a_l T(s_0) T(s_1) = \sum_{i=1}^{p} (1-Q) a_i \boldsymbol{e}_i \tag{13}$$

where $\sum_{i=1}^{p} a_i = 1$ and $\forall i$: $a_i \geq 0$.

E. Shadow MLM Model

The shadow MLM (SMLM) model [29] extends the MLM model from [28] in order to deal with shadows. It is assumed that shadowed regions do not receive direct sunlight but only multiple reflections of direct sunlight. The SMLM model uses the parameter Q to represent the shadow fraction within a pixel. Thus, the light paths and probabilities of the SMLM model are the same as those of the MLM model except for the first order, which is rescaled with $(1 - Q)$, hereby subtracting the shadow

fraction from the direct sunlight term in a spectrum. Thus

$$\begin{aligned}\boldsymbol{x} &= \sum_{L=1}^{1}\left(\sum_{i_1=1}^{p}\cdots\sum_{i_L=1}^{p}\right)(1-Q)(1-P)\prod_{k=1}^{L}(a_{i_k}\boldsymbol{e}_{i_k}) \\ &\quad+\sum_{L=2}^{\infty}\left(\sum_{i_2=1}^{p}\cdots\sum_{i_L=1}^{p}\right)(1-P)P^{L-1}\prod_{k=2}^{L}(a_{i_k}\boldsymbol{e}_{i_k}) \\ &= (1-Q)(1-P)\sum_{i=1}^{p}a_i\boldsymbol{e}_i \\ &\quad+(1-P)P\sum_{i=1}^{p}\sum_{j=1}^{p}a_ia_j\boldsymbol{e}_i\odot\boldsymbol{e}_j+\cdots \\ &= \frac{(1-P)\sum_{i=1}^{p}a_i\boldsymbol{e}_i}{1-P\sum_{i=1}^{p}a_i\boldsymbol{e}_i}-Q(1-P)\sum_{i=1}^{p}a_i\boldsymbol{e}_i \end{aligned} \tag{14}$$

F. Mixture Model With Multiple Light Sources

The work in [39] allows different illumination conditions in sunlit and shadowed regions and regards the shadow effect in a wavelength-dependent manner. In this work, sunlit areas receive the entire solar radiation, i.e., direct as well as diffuse solar radiation, whereas the shadowed regions only receive diffuse radiation. Hence, in the graph representation, two illumination sources, each with its own state, are considered: global radiation $s_{0_{\text{glob}}}$ and diffuse radiation $s_{0_{\text{diff}}}$. Specifically, $s_{0_{\text{glob}}}$ is equivalent to s_0, where only one illumination source is considered. The model accounts for the light paths from the global radiation up to the second order, leading to two possible light paths: $P\left(\text{path}_{\text{glob}}\right)=P(X_0=s_{0_{\text{glob}}},X_1=s_1,X_2=o)=(1-Q)a_l$ for $L=1$ and $P\left(\text{path}_{\text{glob}}\right)=P(X_0=s_{0_{\text{glob}}},X_1=s_1,X_2=s_2,X_3=o)=a_ma_n$ for $L=2$. The spectral contribution of two light paths is $T(s_{0_{\text{glob}}})\prod_{k=1}^{L}\boldsymbol{e}_k$, with $L=1$ and $L=2$, respectively. Moreover, the model assumes that diffuse solar radiation interacts not more than once with ground materials, resulting in the light path $P(\text{path}_{\text{diff}})=P(X_0=s_{0_{\text{diff}}},X_1=s_1,X_2=o)=Qa_l$, where $L=1$ and Q is the spatial fraction of shadow in a pixel. The spectral contribution is $\prod_{k=0}^{L}T(s_{0_{\text{diff}}})\prod_{k=1}^{L}\boldsymbol{e}_l$, where $L=1$. Since the light paths at the second order ($L=2$) is equivalent to the Fan model, we refer to this model as the Fansky model in this article. From (5) follows that $T(s_{0_{\text{diff}}})=\frac{\boldsymbol{\tau}_{\text{diff}}\odot\boldsymbol{E}_s}{\boldsymbol{\tau}_{\text{dir}}\odot\boldsymbol{E}_l+\boldsymbol{\tau}_{\text{diff}}\odot\boldsymbol{E}_s}$. Then, the mixture model can be written as the contribution of all possible light paths, initiated from two illumination sources

$$\begin{aligned}\boldsymbol{x} &= \sum_{L=1}^{2}\left(\sum_{s_{0_{\text{glob}}}\in S}\cdots\sum_{s_L\in S}\right)P\left(\text{path}_{\text{glob}}\right)T\left(s_{0_{\text{glob}}}\right)\prod_{k=1}^{L}T\left(s_k\right) \\ &\quad+\sum_{L=1}^{1}\left(\sum_{s_{0_{\text{diff}}}\in S}\cdots\sum_{s_L\in S}\right)P\left(\text{path}_{\text{diff}}\right)T\left(s_{0_{\text{diff}}}\right)\prod_{k=1}^{L}T\left(s_k\right) \\ &= (1-Q)\sum_{i=1}^{p}a_i\boldsymbol{e}_i+\sum_{i=1}^{p}\sum_{j=i}^{p}a_ia_j\boldsymbol{e}_i\odot\boldsymbol{e}_j+Q\sum_{i=1}^{p}a_i\boldsymbol{e}_i' \end{aligned} \tag{15}$$

where $\boldsymbol{e}_i'=\frac{\boldsymbol{\tau}_{\text{diff}}\odot\boldsymbol{E}_s}{\boldsymbol{\tau}_{\text{dir}}\odot\boldsymbol{E}_l+\boldsymbol{\tau}_{\text{diff}}\odot\boldsymbol{E}_s}$ with $\boldsymbol{E}_l$ and $\boldsymbol{E}_s$ are the vector forms of $E_l(\lambda)$ and $E_s(\lambda)$, respectively.

IV. Proposed Method

We propose an extended SMLM (ESMLM) model by allowing multiple illumination sources, i.e., direct and diffuse solar radiation. Moreover, apart from the optical interactions occurring in a ground pixel determined by its IFOV, a pixel can also receive additional illumination from its neighboring pixels through secondary reflections. Fig. 1 depicts the occurring optical interactions for five different scenarios that are considered in this model. As the path radiance is assumed to be removed by atmospheric correction [7], the model describes three types of light paths, corresponding to three illumination sources: 1) global solar illumination $s_{0_{\text{glob}}}$, diffuse solar illumination $s_{0_{\text{diff}}}$, and neighboring illumination s_{0_N}. The light paths together with their probabilities and spectral contributions for the three illumination sources in the proposed model are presented in Table III, followed by the physical assumptions and a detailed explanation for each illumination source in the remaining part of this section. In brief, the mixture model is computed as the sum of the contributions from all illumination sources in (16) and (17) and contains the following four physically explainable parameters.

1) P: The probability that a light ray undergoes additional interactions with endmembers.
2) Q: The spatial fraction of shadow.
3) F: The sky view factor.
4) K: A strength factor of neighbor interactions, denoting the fraction of the scattered light from the neighborhood that is received by the pixel

$$\begin{aligned}\boldsymbol{x} &= \sum_{L=1}^{2}\left(\sum_{s_{0_{\text{glob}}}\in S}\cdots\sum_{s_L\in S}\right)P\left(\text{path}_{\text{glob}}\right)T\left(s_{0_{\text{glob}}}\right)\prod_{k=1}^{L}T\left(s_k\right) \\ &\quad+\sum_{L=1}^{1}\left(\sum_{s_{0_N}\in S}\cdots\sum_{s_L\in S}\right)P\left(\text{path}_N\right)T\left(s_{0_N}\right)\prod_{k=1}^{L}T\left(s_k\right) \\ &\quad+\sum_{L=1}^{1}\left(\sum_{s_{0_{\text{diff}}}\in S}\cdots\sum_{s_L\in S}\right)P\left(\text{path}_{\text{diff}}\right)T\left(s_{0_{\text{diff}}}\right)\prod_{k=1}^{L}T\left(s_k\right) \\ &= (1-Q)(1-P)\sum_{i=1}^{p}a_i\boldsymbol{e}_i+P\sum_{i=1}^{p}\sum_{j=1}^{p}a_ia_j\boldsymbol{e}_i\odot\boldsymbol{e}_j \\ &\quad+(1-Q)(1-P)K\sum_{i=1}^{p}a_i\boldsymbol{e}_i\odot\boldsymbol{e}_N+QT\left(s_{0_{\text{diff}}}\right)\sum_{i=1}^{p}a_i\boldsymbol{e}_i. \end{aligned} \tag{16}$$

In sunlit regions, the global solar illumination $s_{0_{\text{glob}}}$ is the main illumination source, and the proposed model retains most of the assumptions for $s_{0_{\text{glob}}}$ made by the SMLM model. One difference is that we constrain the parameter P within [0,1], in order to preserve its physical interpretation. Moreover, with the aim of keeping all types of nonlinear interactions up to the same order, the proposed model limits nonlinear interactions of an

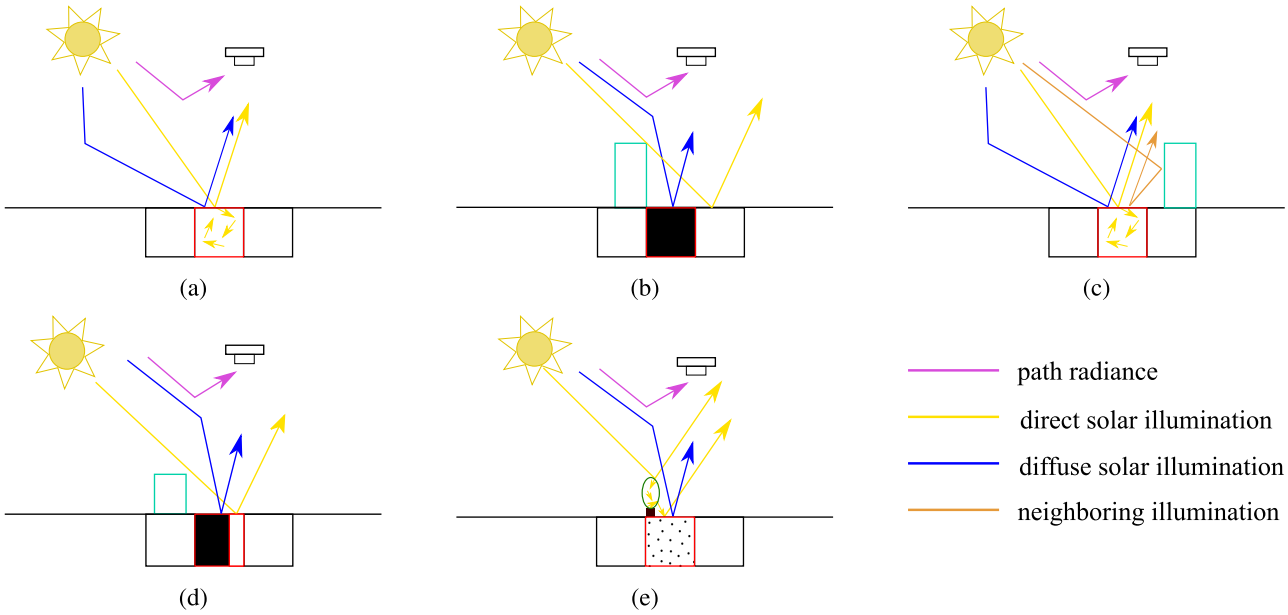

Fig. 1. Solar radiation paths when a pixel is (a) exposed to direct sunlight; (b) fully shadowed; (c) receiving secondary illumination from neighbors; (d) partly shadowed with sunlit and shadowed regions spatially separated in a pixel; (e) partly shadowed with sunlit and shadowed regions not spatially separable in a pixel.

TABLE III
PROBABILITIES OF LIGHT PATHS AND THEIR SPECTRAL CONTRIBUTIONS IN THE PROPOSED MODEL

Path Category	Path	Probability	Contribution	Parameters
$\text{Path}_{\text{glob}}$	$s_{0_{\text{glob}}} - \boldsymbol{e}_i - o$	$(1-Q)(1-P)a_i$	$\boldsymbol{e}_i$	$P, Q, K \in [0,1]$
	$s_{0_{\text{glob}}} - \boldsymbol{e}_i - \boldsymbol{e}_j - o$	Pa_ia_j	$\boldsymbol{e}_i \odot \boldsymbol{e}_j$	
$\text{Path}_{\text{diff}}$	$s_{0_{\text{diff}}} - \boldsymbol{e}_i - o$	Qa_i	$T(s_{0_{\text{diff}}}) \cdot \boldsymbol{e}_i$	
Path_N	$s_{0_N} - \boldsymbol{e}_i - o$	$(1-Q)(1-P)a_i$	$K\boldsymbol{e}_N \odot \boldsymbol{e}_i$	

incoming light ray up to the second order. In the specific, the following assumptions for $s_{0_{\text{glob}}}$ are made.

1) An incoming light ray from the global illumination source will interact with at least one material in a pixel. After each interaction with a material, the ray will have probabilities P and $(1-P)$ of undergoing further interactions within the current pixel or escaping the current pixel, respectively.
2) As the shadowed part of a pixel does not have a direct line of sight to the sun, the probability that the reflected light escapes a partly shadowed pixel after the first interaction is rescaled with $(1-Q)$, with $Q \in [0,1]$ the fractional value of the shadow in the pixel. Thus, after the first interaction with a material, the light ray will have a probability $(1-Q)(1-P)$ of escaping the current pixel. On the other hand, the shadowed part of a pixel can receive reflected light from $s_{0_{\text{glob}}}$, thus the probability of a secondary reflection remains P without rescaling with $(1-Q)$.

These assumptions for the global illumination source lead to two possible light paths: $P\left(\text{path}_{\text{glob}}\right) = P(X_0 = s_{0_{\text{glob}}}, X_1 = s_1, X_2 = o) = (1-Q)(1-P)a_l, (l = 1, \ldots, p)$ for $L = 1$ and $P\left(\text{path}_{\text{glob}}\right) = P(X_0 = s_{0_{\text{glob}}}, X_1 = s_1, X_2 = s_2, X_2 = o) = Pa_ma_n, (m, n = 1, \ldots, p)$ for $L = 2$. The spectral contribution of these two light paths is $T\left(s_{0,\text{glob}}\right) \prod_{k=1}^{L} \boldsymbol{e}_k$, with $L = 1$ and $L = 2$, respectively.

In addition to receiving global illumination, the target pixel receives secondary reflections from its neighborhood. The neighbor illumination source s_{0_N} follows the following assumptions.

1) By keeping all types of nonlinear effects up to the second order, only neighboring regions having a direct view of the sun can contribute to the target pixel. Thus, the neighboring effect corresponds to the reflected light of a pixel after receiving the global illumination $s_{0_{\text{glob}}}$.
2) Following the Lambertian law, by escaping the pixel, the scattered light ray from $s_{0_{\text{glob}}}$ is reflected in all directions, including toward the sensor and neighboring pixels, with equal probability of $(1-Q)(1-P)$.
3) By assuming a homogeneous local neighborhood, the probability that a pixel scatters light to its neighboring pixels is equal to the probability that the neighboring pixels scatter light to the pixel, and is given by $(1-Q)(1-P)$.
4) We define an additional parameter $K \in [0,1]$, i.e., a strength factor of neighbor interactions, denoting the fraction of the scattered light from the neighborhood that is received by the pixel.

Thus, the probability of the light paths, corresponding to the neighbor illumination source are: $P(\text{path}_N) = P(X_0 = s_{0_N}, X_1 = s_1, X_2 = o) = (1-Q)(1-P)a_l, (l = 1, \ldots, p)$ for $L = 1$. The spectral contribution is $T(s_{0_N}) \prod_{k=1}^{L} \boldsymbol{e}_k$ where $T(s_{0_N}) = \boldsymbol{e}_N$. The neighborhood is defined by a radius R. The neighborhood spectrum $\boldsymbol{e}_N(i,j)$ of target pixel $\boldsymbol{x}(i,j)$ is

computed as the average spectrum of its neighboring pixels, weighted by their inverse distance to the target

$$\boldsymbol{e}_N(i,j) = \frac{\sum_{s=-R}^{R}\sum_{t=-R}^{R}\boldsymbol{x}(i+s,j+t)W(s,t)}{\sum_{s=-R}^{R}\sum_{t=-R}^{R}W(s,t)} \quad (17)$$

where $W(s,t) = \frac{\delta}{D((i,j),(i+s,j+t))}$ and D denotes the Euclidean distance between two pixels in the spatial domain. Since only neighboring regions having a direct view of the sun can contribute to the target pixel, we exclude (partly) shadowed pixels when computing $\boldsymbol{e}_N$, by using the δ symbol, where $\delta = 1$ in full sunlit pixels with $Q < 0.1$, and $\delta = 0$ otherwise.

Last but not least, the diffuse solar illumination $s_{0_{\text{diff}}}$ plays an important role in shadowed regions. The diffuse solar illumination is the scattered light by the atmosphere in all directions. Since we aim to keep all types of nonlinear interactions up to the same order, i.e., the second order, we regard only the linear interactions for $s_{0_{\text{diff}}}$. In the proposed model, the following assumptions hold for $s_{0_{\text{diff}}}$.

A light ray from the diffuse solar illumination source will interact with at least one material. After the first interaction, the light ray will escape the pixel with a fraction of Q and reach the observer.

Hence, the light path corresponding to the diffuse solar illumination source is $P(\text{Path}_{\text{diff}}) = P(X_0 = s_{0_{\text{diff}}}, X_1 = s_1, X_2 = o) = Qa_l, (l = 1, \ldots, p)$ with the spectral contribution for $L = 1$. The spectral contribution is $T(s_{0_{\text{diff}}})\prod_{k=1}^{L}\boldsymbol{e_i}$ where $T(s_{0_{\text{diff}}}) = \frac{\boldsymbol{\tau}_{\text{diff}}\odot\boldsymbol{E}_s}{\boldsymbol{\tau}_{\text{dir}}\odot\boldsymbol{E}_l+\boldsymbol{\tau}_{\text{diff}}\odot\boldsymbol{E}_s}$.

V. Experimental Setup

This section introduces three datasets to evaluate the spectral mixing methods quantitatively or qualitatively by considering the shadow and nonlinear effects. One difficulty for the quantitative evaluation of the shadow-aware unmixing methods is that the ground truth of abundances and shadow fractions is not available and very difficult to acquire in the case of shadows. Thus, we first validate our method on a simulated dataset with known abundances and parameters for a quantitative evaluation of the performance of the mixture models. Furthermore, we compare the unmixing methods on a real image with simulated shadowed pixels. Finally, we show experimental results on real airborne hyperspectral imagery without ground truth data, both quantitatively and qualitatively.

A. Datasets

1) Synthetic Dataset: Considering that a validation dataset with (partly) shadows is not available and very difficult to acquire, we validate our method on a simulated dataset to evaluate the mean reconstruction error RE and mean abundance error AE quantitatively. We randomly select 10 endmembers from the United States Geological Survey (USGS) spectral library of minerals,[1] where each material comprises 224 spectral bands ranging from 383 nm to 2508 nm. Abundances are then randomly generated following the Dirichlet distribution that automatically enforces the ANC and ASC constraints. Then, hyperspectral data are generated following each of the considered mixing models, i.e., LMM, Fan, SLMM, SMLM, Fansky and the proposed ESMLM. Parameters P are randomly generated based on the half-normal distribution with $\delta = 0.3$. Values larger than one are set to zero, following the work in [28]. Other parameters including $Q \in [0,1], F \in [0,1], K \in [0,1], \gamma \in [0,1], b \in [-1,1]$ are generated following the uniform distribution. k_1, k_2, k_3 are chosen the same as the ones used for the real hyperspectral imagery in Section V-C. Furthermore, we add white noise with signal-to-noise ratios SNR $= [50, 100]$ to the simulated dataset to assess the noise impact on different unmixing methods.

[1][Online]. Available: https://speclab.cr.usgs.gov/spectral-lib.html

TABLE IV
Ground Truth of Abundances in the HySU Dataset

Endmember	Target area [pixel]
bitumen	18.429
red-painted metal sheets	18.061
blue fabric	18.245
red fabric	18.798
green fabric	18.521
Total	92.054

2) Real Dataset: DLR HyperSpectral Unmixing Benchmark Dataset: The image was acquired over Oberphaffenhofen, Bavaria, Germany with a HySpex pushbroom camera, resulting in a ground sampling distance of 0.7 m. The image comprises 135 spectral bands ranging from 417.4 nm to 902.8 nm. This dataset [43] contains ground targets with five materials (bitumen, red-painted metal sheets, blue fabric, red fabric, and green fabric) and the background material (grass), thus a total of six endmembers are known from the dataset. In our experiment, we use targets with side lengths of 3 m, and the target area can be translated in a number of pixels in the image and is going to be used as the ground truth for the abundances (see Table IV). Fig. 2 shows the hyperspectral image as true-color composite and the endmembers.

In order to validate shadow-aware models quantitatively, we simulate shadows partially covering the shadow-free image in Fig. 2(a). First, we manually draw a shadowed region in the center of the image to shade a part of all targets, resulting in a binary shadow mask. Then, we apply a Gaussian filter with size $3 * 3$ to the shadow mask and generate a soft shadow mask Q [see Fig. 2(d)]. After that, given a pixel $\boldsymbol{y}_i$ in the real image, we simulate the shadow-included image in Fig. 2(c) using (18). $T_{s_{0,\text{diff}}}$ is computed with $F = 1$ based on the field knowledge, and parameters k_1, k_2, k_3 are set as in Section V-C

$$\boldsymbol{x}_i = (1 - Q_i)\boldsymbol{y}_i + Q_i T_{s_{0_{\text{diff}}}}\boldsymbol{y}_i. \quad (18)$$

It is worth noticing that (18) implicitly embeds nonlinear effects contained in pixel $\boldsymbol{y}_i$, so we do not add additional nonlinear effects in this image. However, since the study area is located in the middle of a field with flat terrain, and we quantitatively validate solely the abundances of the ground targets made of synthetic materials, the nonlinear effect plays a minor role (see Table VIII and Fig. 5).

3) Real Dataset: Airborne Hyperspectral Imagery: A real airborne hyperspectral image [see Fig. 3(a)] is selected from a scene acquired over Oberpfaffenhofen, Bavaria, Germany

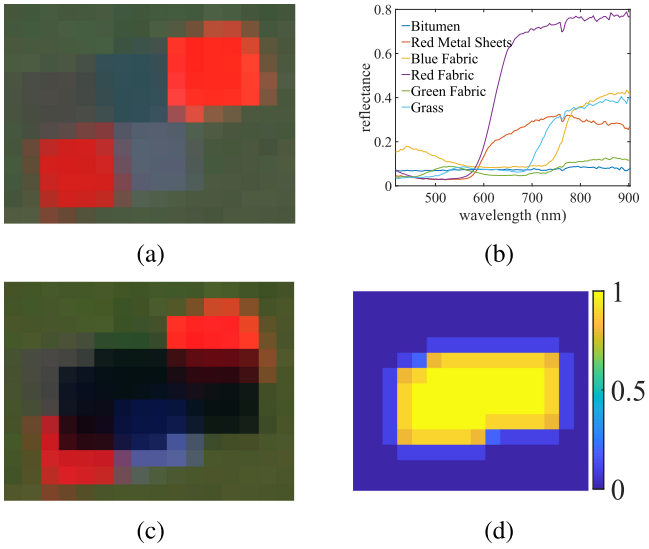

Fig. 2. DLR HySU dataset with simulated shadowed pixels. (a) Hyperspectral image as a true color composite including five ground targets with side lengths of 3 m. (b) Endmember library containing five ground materials (bitumen, red-painted metal sheets, blue fabric, red fabric, and green fabric) and grass. (c) Hyperspectral image with simulated shadowed pixels. (d) Soft shadow map.

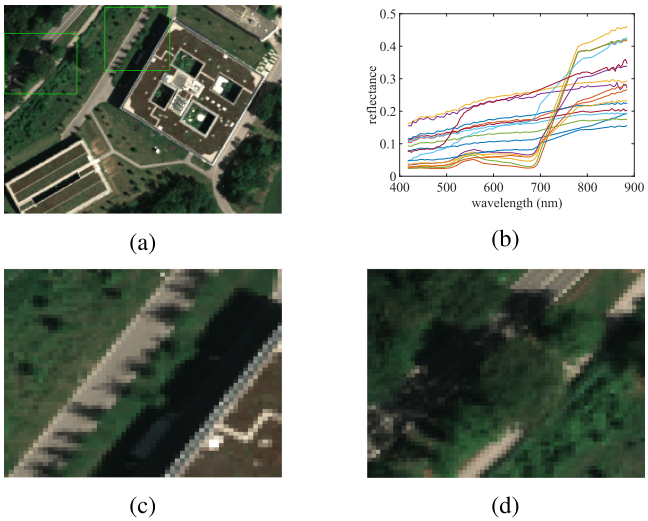

Fig. 3. Hyperspectral dataset. (a) Hyperspectral image as a true color composite acquired by the HySpex sensor in the study area of Oberpfaffenhofen, Bavaria, Germany. (b) Endmember library, manually selected from (a). (c) and (d) True color composites of subsets selected from image (a).

between 8:42 and 8:56 A.M. (Central European Summer Time) on June 4, 2018 with a HySpex VNIR sensor [44], flying at an altitude of 1615 m above ground level, resulting in a ground sampling distance of 0.7 m. The image comprises 160 spectral bands ranging from 416 to 988.4 nm and has been atmospherically corrected using ATCOR [6]. After removing water vapor bands, a total of 101 bands have been kept for further processing. A spectral library of endmembers is generated by manually selecting pure pixels of relevant materials in fully sunlit pixels of the image [see Fig. 3(b)]. We select endmembers manually, as the endmembers should be extracted from fully sunlit pixels.

TABLE V
RUNNING TIME OF COMPARED MODELS IN THE TWO SUBSETS

Model	Running time (s)	
	subset1 (3135 pixels)	subset 2 (3328 pixels)
LMM	26.04	20.71
Fan	55.89	41.99
SLMM	34.23	24.50
SMLM	57.47	45.31
Fansky	522.28	381.49
ESMLM	203.72	204.83

In other words, to be able to use an automatic endmember extraction method, one would have to find a shadow detection method that can distinguish fully sunlit pixels from other pixels with ideally 100% accuracy, which is not easy to achieve in reality. For validation and comparison of the proposed model, we selected two subsets from the entire image [see Fig. 3(c) and (d)], which are dominated by shadow effects and cover three different shadow types, described in Fig. 1(b),(d), and (e).

B. Quantitative Measures

For validation and comparison, a number of quantitative measures have been applied. Denote $\boldsymbol{x}_i$ and $\hat{\boldsymbol{x}}_i$ as the observed and reconstructed spectrum, respectively, of pixel i, where $\boldsymbol{x}_i = [x_{i,\lambda_1}, x_{i,\lambda_2}, \ldots, x_{i,\lambda_d}]$ and $\hat{\boldsymbol{x}}_i = [\hat{x}_{i,\lambda_1}, \hat{x}_{i,\lambda_2}, \ldots, \hat{x}_{i,\lambda_d}]$. The mean reconstruction error RE is written as

$$\text{RE} = \frac{1}{N}\sum_{i=1}^{N}\sqrt{\sum_{j=1}^{d}\left(x_{i,\lambda_j} - \hat{x}_{i,\lambda_j}\right)^2}. \tag{19}$$

In order to evaluate the spectral behavior of the reconstruction errors, we calculate the spectral reconstruction error SRE as a function of wavelength λ, averaged over N pixels

$$\text{SRE}(\lambda) = \frac{1}{N}\sum_{i=1}^{N}|x_{i,\lambda} - \hat{x}_{i,\lambda}|. \tag{20}$$

In addition, the mean abundance error (AE) is computed as

$$\text{AE} = \frac{1}{pN}\sum_{i=1}^{N}\sum_{j=1}^{p}|a_{i,j} - \hat{a}_{i,j}|. \tag{21}$$

C. Unmixing Procedure

In this article, we compare the proposed model (ESMLM) with the following state-of-the-art mixture models: LMM [13], Fan [22], SLMM [28], SMLM [29], and Fansky [39].

All algorithms were developed in MATLAB and run on an Intel Core i7-8650 U CPU, 1.90-GHz machine with 4 Cores and 8 Logical Processors. We use the MATLAB function FMINCON to perform the nonlinear optimization. The processing time depends on the number of input pixels and endmembers. Table V shows the running time of the compared models in the two subsets of the real airborne hyperspectral imagery. The function and constraint tolerance are set to 10^{-10} and 10^{-8}, respectively. The initial values of the abundances are set to $\frac{1}{p}$ and the initial values of the unknown parameters F, Q, P, K are set to [1,1,0,0].

For the methods considering skylight, i.e., the Fansky and ESMLM model, 10 pairs of pixels have been selected in the

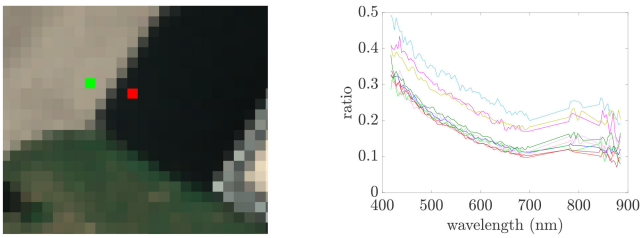

(a) (b)

Fig. 4. Selection of 10 pairs of sunlit and shadowed pixels. (a)Example of the pixel selection for computing parameters k_1, k_2, and k_3. (b) Ratios computed from 10 pairs of pixels.

scene to compute the parameters k_1, k_2, and k_3 by using (6). Specifically, we select fully sunlit and shadowed pixels of the same pure material on the high-resolution hyperspectral image, assuming that two pixels near a shadow boundary are composed of the same material. Besides, we avoid vegetation materials during the pixel selection to avoid nonlinear effects. Fig. 4(a) shows an example of selecting one pair of pixels. Fig. 4(b) presents the ratios computed by 10 pairs of fully sunlit and fully shadowed pixels. Assuming that the atmospheric conditions are constant in the entire region, these parameters are assumed to be constant and were set as $k_1 = 1.296$; $k_2 = 6.068$; $k_3 = 0.442$.

D. Experimental Design

Experimental results are shown in the following sections. In Section VI, we perform a quantitative analysis of the RE and AE on the synthetic dataset simulated by the USGS spectral library. In Section VII, we evaluate the unmixing results on the DLR HyperSpectral Unmixing (HySU) dataset [43]. Specifically, the five ground targets are used to validate abundance errors. Section VIII evaluates the spectral mixing models on the real hyperspectral imagery without ground truth data, quantitatively and qualitatively. In Section VIII-A, we perform a quantitative analysis of the spatial and spectral reconstruction errors. Moreover, we generate shadow-removed images in Section VIII-B. This can be achieved by "lightening up" the shadow fraction in a mixture model, if applicable. Some of the unmixing methods output physically interpretable parameters, which provide valuable information about the observed surface. We discuss qualitative results of output parameters and abundances in Sections VIII-C and VIII-D. In Section VIII-E, we conduct an ablation study of the proposed model and analyze the impact of each parameter on the experimental results. Section VIII-F discusses the impact of endmember extraction methods on the unmixing results. Finally, we demonstrate our proposed model on the entire test image in Section VIII-G.

VI. Synthetic Dataset

Tables VI and VII present the mean reconstruction error (RE) and mean abundance error (AE) of mixture models at different noise level following (19) and (21), respectively. The columns represent the spectral mixture models according to which mixtures are generated, and the rows correspond to the methods that were used to unmix the data. The last column conveys the mean performance of each unmixing method for all types of generated mixtures. For each type of mixture, the first and second best unmixing methods have been highlighted in red and green colors, respectively. For all mixtures generated by the different models, the proposed unmixing method obtained the best or second-best RE and AE among all comparing methods and achieved the best results on average. Results indicate that the ESMLM model can tackle different kinds of mixtures.

TABLE VI
Mean Reconstruction Error (RE) for the Synthetic Dataset

Noiseless	LMM	Fan	SLMM	SMLM	Fansky	ESMLM	Mean
LMM	0	0.9134	1.219	1.133	0.731	0.865	0.810
Fan	0.125	0	1.318	1.235	0.721	0.895	0.716
SLMM	0	0.913	0	0.122	0.262	0.248	0.258
SMLM	0	0.913	0.007	0.005	0.232	0.216	0.229
Fansky	0.054	0	0.050	0.052	0	0.060	0.036
ESMLM	0.002	0.050	0	0.013	0.018	0.002	0.014
SNR100	LMM	Fan	SLMM	SMLM	Fansky	ESMLM	Mean
LMM	0	0.915	0.038	0.242	0.723	0.606	0.421
Fan	0.124	0	0.159	0.353	0.043	0.232	0.152
SLMM	0	0.915	0	0.111	0.723	0.589	0.390
SMLM	0	0.915	0	0	0	0.565	0.367
Fansky	0.053	0	0.053	0.048	0	0.129	0.047
ESMLM	0.003	0.045	0.001	0.008	0.034	0.006	0.016
SNR50	LMM	Fan	SLMM	SMLM	Fansky	ESMLM	Mean
LMM	0.029	0.916	0.043	0.243	0.723	0.607	0.427
Fan	0.128	0.035	0.160	0.353	0.051	0.234	0.160
SLMM	0.029	0.916	0.017	0.114	0.723	0.590	0.398
SMLM	0.029	0.916	0.017	0.016	0.723	0.567	0.378
Fansky	0.061	0.035	0.056	0.052	0.022	0.134	0.060
ESMLM	0.029	0.064	0.017	0.020	0.045	0.029	0.034

TABLE VII
Mean Abundance Error AE for the Synthetic Dataset

Noiseless	LMM	Fan	SLMM	SMLM	Fansky	ESMLM	Mean
LMM	0	0.082	0.121	0.126	0.096	0.104	0.088
Fan	0.049	0	0.138	0.139	0.101	0.115	0.090
SLMM	0	0.082	0	0.031	0.044	0.046	0.034
SMLM	0	0.082	0.010	0.006	0.044	0.046	0.031
Fansky	0.032	0	0.067	0.036	0	0.031	0.028
ESMLM	0.001	0.010	0	0.007	0.013	0	0.005
SNR100	LMM	Fan	SLMM	SMLM	Fansky	ESMLM	Mean
LMM	0	0.082	0.121	0.126	0.096	0.104	0.088
Fan	0.049	0	0.137	0.139	0.101	0.115	0.090
SLMM	0	0.082	0	0.031	0.044	0.046	0.034
SMLM	0	0.082	0.010	0.006	0.044	0.046	0.031
Fansky	0.032	0	0.067	0.036	0	0.031	0.028
ESMLM	0	0.010	0	0.007	0.013	0	0.005
SNR50	LMM	Fan	SLMM	SMLM	Fansky	ESMLM	Mean
LMM	0.001	0.082	0.121	0.126	0.096	0.104	0.088
Fan	0.049	0.001	0.137	0.139	0.101	0.115	0.090
SLMM	0.001	0.082	0.004	0.031	0.044	0.046	0.035
SMLM	0.001	0.082	0.014	0.008	0.044	0.046	0.033
Fansky	0.032	0.001	0.067	0.036	0.001	0.031	0.028
ESMLM	0.002	0.010	0.005	0.008	0.014	0.003	0.007

VII. Real Dataset: HySU

Fig. 5 presents the obtained RE in fully sunlit pixels, (partly) shadowed pixels, and the entire image, respectively, and Table VIII compares the AE of the ground targets made of synthetic materials.

In fully sunlit pixels, reconstruction errors of linear and nonlinear models are similar, indicating that the nonlinear effect plays a minor role in the study scene. On the other hand, RE largely varies in (partly) shadowed pixels. When the shadow effect is taken into account, RE significantly decreases in (partly)

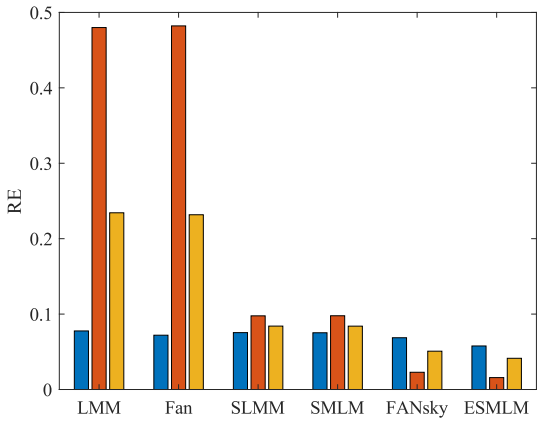

Fig. 5. Mean reconstruction error RE of fully sunlit pixels (in blue), (partly) shadowed pixels (in orange), and the entire image (in yellow) in HySU dataset. Fully sunlit and (partly) shadowed pixels are identified as $Q \leq 0.1$ and $Q > 0.1$, respectively.

TABLE VIII
ABUNDANCE ERROR IN NUMBER OF PIXELS IN THE HYSU DATASET

Endmember	LMM	Fan	SLMM	SMLM	Fansky	ESMLM
bitumen	50.422	53.184	43.019	43.430	9.504	1.366
red-painted metal sheets	6.529	6.051	2.234	2.286	4.097	0.702
blue fabric	12.232	12.299	10.234	10.356	0.837	0.108
red fabric	9.111	9.932	7.570	7.628	3.719	0.443
green fabric	6.471	6.229	10.020	10.029	1.832	2.614
Total	84.765	87.695	73.076	73.728	19.989	5.233
Total(%)	92.08	95.26	79.38	80.09	21.71	5.68

shadowed pixels and the lowest reconstruction errors are obtained when considering the skylight.

Using the ground truth data from Table IV, the total number of pixels for each material is representative for the total corresponding abundance in the image. Thus, we represent the abundance estimation error by the absolute difference in number of pixels between ground truth and estimated values over the five targets (see Table VIII). In addition, we present the total (absolute and in percentage) estimation error by summing up the errors of all endmembers. Besides, we compare abundance maps qualitatively for all materials in Fig. 6, where the first column shows the reference abundance maps for easier comparison. Specifically, the reference abundance maps are estimated using the shadow-free image through nonnegative least squares.

In sunlit regions, the LMM and the Fan model estimate correct abundances, but show high abundance estimation errors compared to other methods in (partly) shadowed pixels. Among all materials, the largest abundance error appears in bitumen, which has a relatively small reflectance and is, therefore, easily confused with shadows. Besides, more confusion between similar materials can be observed. An example appears in shadowed pixels of grass, where the LMM and Fan models confuse those regions with green fabric.

Compared with the LMM and the Fan model, the SLMM and SMLM model perform slightly better. In partly shadowed pixels, the SLMM and the SMLM model detect part of the correct materials. However, some shadowed pixels of red fabric, which have been estimated as bitumen by the LMM and Fan model, are confused with red metal sheets.

The Fansky and ESMLM models outperform SLMM and SMLM for the abundance estimation of all ground targets, indicating that the wavelength-dependent skylight information cannot be well represented using a scaling parameter. Most shadowed pixels have been detected as the correct material, resulting in largely decreased abundance estimation errors. The Fansky model confuses between materials with similar spectra, such as green fabric and grass, as well as red fabric and red metal sheets. In addition, it confuses blue materials with bitumen. Compared to other models, the ESMLM model achieves the best performance and can detect most ground targets with a total abundance estimation error of 5.233 pixels (corresponding to 5.68%). Specifically, the ESMLM model can better identify similar materials in shadowed pixels thanks to the advantageous and flexible modeling of nonlinear effects.

VIII. Real Dataset: Airborne Hyperspectral Imagery

A. Reconstruction Errors

The mean reconstruction errors RE (19) of each of the two subsets for all compared methods is depicted in Fig. 7. Separate results are shown for fully sunlit, (partly) shadowed pixels, and the entire image, respectively. (Partly) shadowed pixels are identified using $Q > 0.1$, whereas fully sunlit pixels are identified using $Q \leq 0.1$, where Q values are computed using the proposed model. Results suggest that reconstruction errors highly depend on if and how the models consider the illumination conditions and the nonlinearity. In (partly) shadowed pixels, the reconstruction errors largely decrease when using shadow-aware mixture models, i.e., the SLMM, SMLM, Fansky, and ESMLM models. Among all shadow-aware models, the Fansky and ESMLM models consider the skylight information and thus outperform other models. Compared to the Fansky model, ESMLM obtained the smallest reconstruction errors in (partly) shadowed pixels, especially when areas are shaded by vegetation, such as in subset 2. Since both models consider skylight information, this implies that the ESMLM model treats the nonlinearity better than the Fansky model in (partly) shadowed pixels. In sunlit regions, the reconstruction errors appear larger in subset 2, where the ground surface is covered mostly by vegetation. The Fan and Fansky models attained slightly lower errors than the linear models but yielded higher errors than the ESMLM model regarding the neighborhood interactions. Overall, the ESMLM model attained the best pixel reconstruction and, in this respect, it produced a better representation of the ground mixtures.

Fig. 8 shows spectral reconstruction errors SRE(λ) (20), which denote how well a spectral mixing model represent input pixels as a function of wavelength. When a mixing model obtains a good spectral representation, we expect the SRE values to be constant and small for all wavelengths. Instead, if SRE largely varies as a function of λ, the spectral unmixing method is not capable of dealing with specific wavelength-dependent effects. As both subsets contain large shadowed regions, the LMM and Fan models obtained the largest errors over the entire wavelength range. The SLMM and SMLM models obtained higher errors in

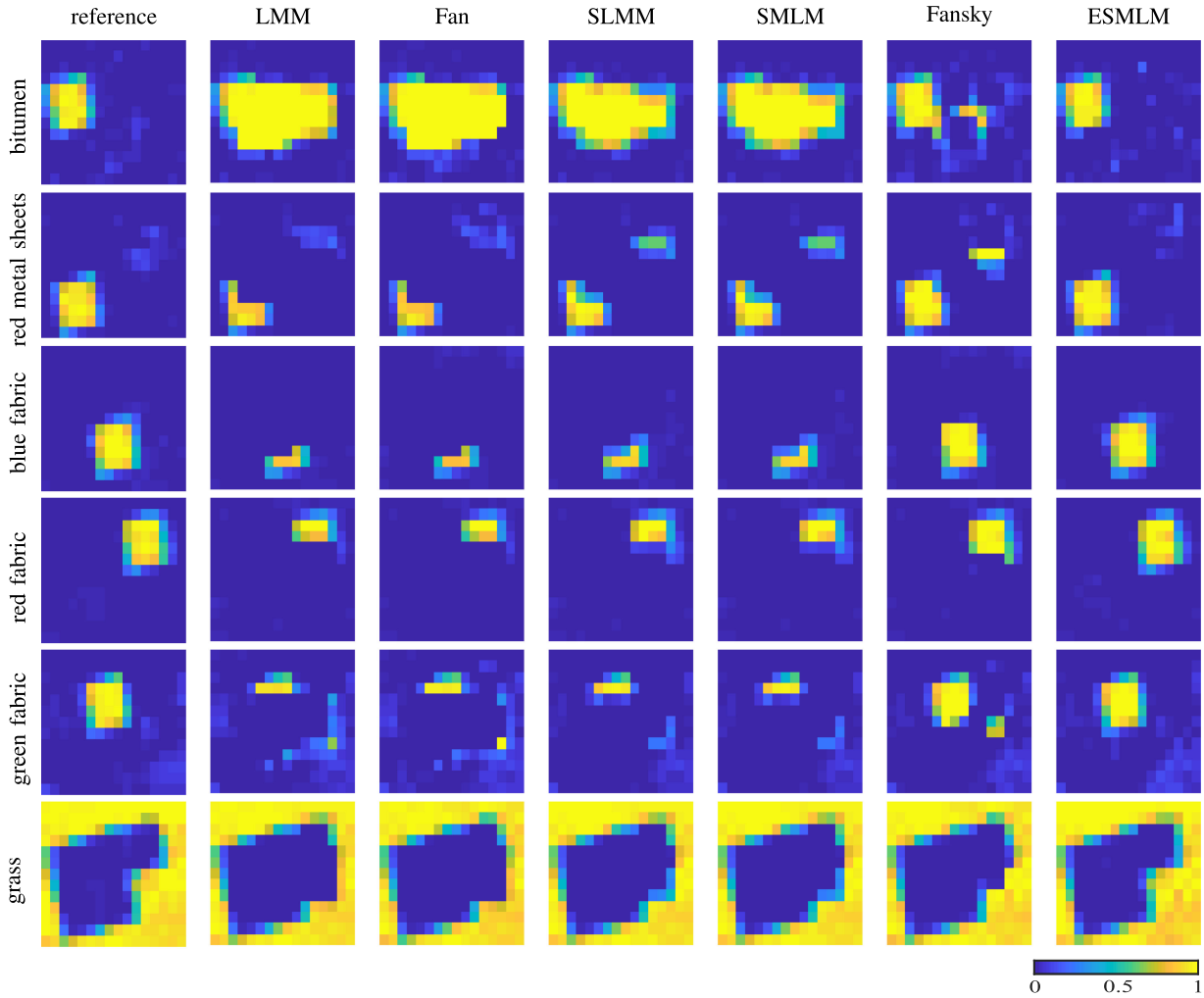

Fig. 6. Abundance maps from the HySU dataset. Top to bottom: Bitumen, red metal sheets, blue fabric, red fabric, green fabric, and grass. Left to right: Reference, LMM, Fan model, SLMM, SMLM model, Fansky model, and ESMLM model. The reference abundance maps are computed using the shadow-free image through nonnegative least squares.

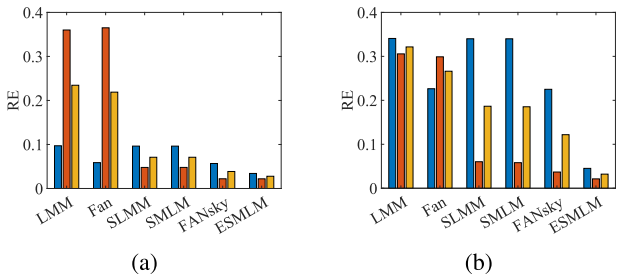

Fig. 7. Mean reconstruction error (RE) of fully sunlit pixels (in blue), (partly) shadowed pixels (in orange), and the entire image (in yellow), for subset 1 in (a) and subset 2 in (b). Fully sunlit and (partly) shadowed pixels are identified as $Q \leq 0.1$ and $Q > 0.1$, respectively, where Q values are computed using the ESMLM model.

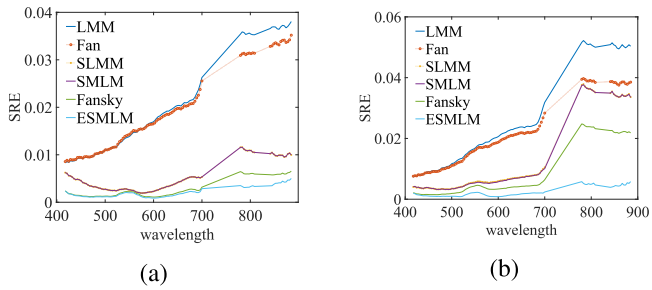

Fig. 8. Spectral reconstruction errors (SRE) as a function of wavelength for subset 1 in (a) and subset 2 in (b).

the lower spectral range of 400–500 nm, because these assume the shadow effects to be wavelength-independent, and ignore the skylight that has the highest impact at shorter wavelengths. In subset 2, the spectral reconstruction errors appear larger at longer wavelengths, and the spectral behavior of the errors shows vegetation characteristics. Compared to the Fansky model, the ESMLM model shows less vegetation characteristics, indicating that it provides a better spectral reconstruction performance for vegetation.

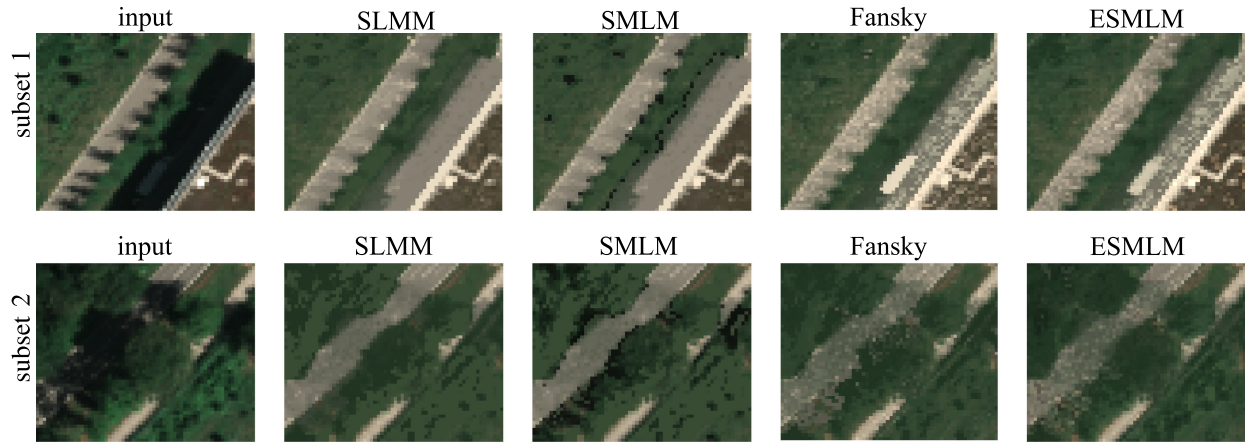

Fig. 9. Shadow-removed reconstructed images (true color composites) of subset 1 (first row) and subset 2 (second row).

B. Shadow-Removed Pixel Reconstruction

For spectral mixture models containing the shadow-related parameter Q, it is possible to perform shadow removal through pixel reconstruction. The idea is to "lighten up" the shadow fraction in a pixel, by replacing the illumination source for shadowed regions with the one for sunlit regions. In other words, the restoration process simulates that shadowed regions are exposed to direct solar illumination. Since SLMM and SMLM models do not contain the diffuse illumination source for shadowed regions, shadow removal can be performed by setting $Q = 0$ in the mixture models. For the Fansky and ESMLM models, we generate the restoration results by replacing $T(s_{0_{\text{diff}}})$ with $T(s_{0_{\text{glob}}})$ in the mixture models. Fig. 9 shows the input and shadow-removed images for visual comparison. Since the shadow removal is performed by replacing the illumination sources in the mixture models, the shadow fraction Q has been naturally embedded in the restoration process, yielding physical-interpretable transitions at shadow boundaries in the shadow-removed images. As the values of Q are fractional in the range [0,1], a more realistic representation of shadows is provided.

Due to the lack of ground truth of the actual spectral reflectance and thus the actual pixel composition under the shadows, the shadow-removed images can only be qualitatively compared. For a more quantitative evaluation of the performance of shadow removal, we additionally designed an alternative test, by assuming that the region around a shadow boundary should contain similar materials (see Fig. 10). In each subset we selected seven regions, each consisting of sunlit pixels (located at the yellow markers) and (partly) shadowed pixels (located at the cyan markers) around a shadow boundary [see Fig. 10(a) and (e)]. Spectra in sunlit pixels are selected from the input image, whereas spectra in (partly) shadowed pixels are selected from the restored image. In each region, the spectra of sunlit and (partly) shadowed pixels are individually averaged, resulting in seven pairs of spectra, each consisting of a sunlit and a shadowed spectrum around a shadow boundary. The bandwise absolute differences between the sunlit and shadowed spectra are averaged over all seven pairs and plotted as the spectral error in Fig. 10(b) and (f). In addition, in subset 1, we individually

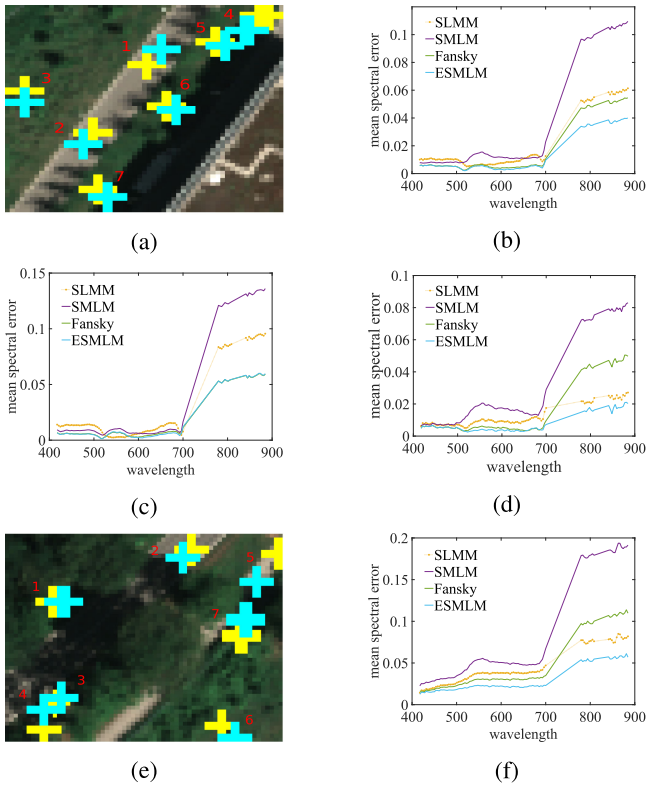

Fig. 10. Spectral comparison between shadowed pixels in shadow-removed images and their corresponding sunlit pixels belonging to the same material in local neighborhoods. Subset 1: (a) Locations of selected pairs of pixels, sunlit pixels are marked in yellow, and (partly) shadowed pixels are marked in cyan. (b) Spectral error (all regions). (c) Spectral error in regions shadowed by man-made objects. (d) Spectral error in regions shadowed by vegetation. Subset 2: (e) Location of selected pairs of pixels, sunlit pixels are marked in yellow and (partly) shadowed pixels are marked in cyan. (f) Spectral error over all regions (all regions are shadowed by vegetation).

consider shadows caused by man-made objects, completely blocking direct sunlight, and shadows caused by vegetation that can partly block direct sunlight [see Fig. 10(c) and (d)].

The visual comparison of Fig. 9 can be interpreted, depending on the skylight information being taken into account or not.

When excluding the skylight information (i.e., SLMM and SMLM models), results show less noise in shadowed restored regions. However, texture and spectral information can be lost in shadow areas, leading to a nonnatural restoration result, and incorrect spectral information of the pixel composition under the shadow. In addition, the SMLM model has not removed all shadows, due to an inaccurate estimation of its parameters (see Section VIII-C).

In contrast, the models that account for skylight show increased noise levels (see Fig. 9) but on average perform better in restoring the spectral information in shadowed pixels (see Fig. 10). The Fansky model behaves inconsistently in different types of shadows. Specifically, it performs worse than SLMM in the regions shadowed by vegetation [see Fig. 10(d) and (f)], probably due to its specific modeling of the nonlinearities. The proposed ESMLM model performs consistently better for different types of shadows, indicating the importance of the nonlinear modeling in shadow-aware mixture models.

C. Model Parameters

Some of the compared spectral mixture models generate physically interpretable pixelwise parameters providing valuable information. Fig. 11 shows the output parameter maps. All compared mixture models, except LMM and FAN, output Q, representing the fraction of shadows at subpixel level. Depending on the way the shadow effect is modeled, two categories of Q maps can be differentiated. The SLMM and the SMLM models treat shadow as a simple scaling effect without including skylight information. Despite Q being the spatial fraction of shadow in a pixel, it serves two functionalities here. One is to reduce the observed reflectance by scaling out the shadowed part Q of a pixel. The other is to use the remaining fractional value $1-Q$ to "lighten up" the shadowed regions. From the figure, on can clearly observe that the Q values from SLMM and SMLM are consistently underestimated in shadowed pixels, because even in heavily shadowed regions, the reflectance, although very small, is not equal to zero. Compared to the SLMM, the SMLM model can underestimate Q in (partly) shadowed pixels by overestimating the P values, such as in vegetation shadows in subset 2 and on the boundaries of the shadowed regions by the building in subset 1. The inaccurate estimation of Q greatly decreases the performance for shadow removal (see Fig. 9). In contrast, the ESMLM and Fansky models use the skylight to "lighten up" the shadowed areas, yielding a better estimation for Q. Compared to the Fansky model, the ESMLM model generates better Q maps, thanks to its superior nonlinear modeling. In subset 2, the ESMLM model estimates higher values of Q in fully shadowed pixels and can detect partial shadows in the bottom right area.

Beside shadows, the nonlinear behavior of the mixture models is also an important aspect. Fig. 11 shows the two parameters relevant to the nonlinearity, i.e., P and K, which describe within- and between-pixel optical interactions at the second order, respectively. The P parameter in the ESMLM model follows the definition from the work in [29]. Although P can be negative in the SMLM model, we constrain $P \in [0, 1]$ in this article in order to keep its physical interpretation. The P maps of SMLM and ESMLM follow similar patterns, with increasing values in vegetated regions. In SMLM, P can have high values in (partly) shadowed pixels where Q is close to zero. This artifact can be observed on shadow boundaries of the building in subset 1, and tree-shadowed regions in both subsets. The ESMLM model shows a better estimation of both P and Q, due to the inclusion of skylight information.

The ESMLM model outputs high values of K, dominantly in (partly) sunlit vegetated areas, where pixels are expected to receive reflections from their neighborhood. Those regions show significantly lower reconstruction errors in the ESMLM model than in other models, indicating the advantage of modeling the neighbor interactions in the ESMLM model.

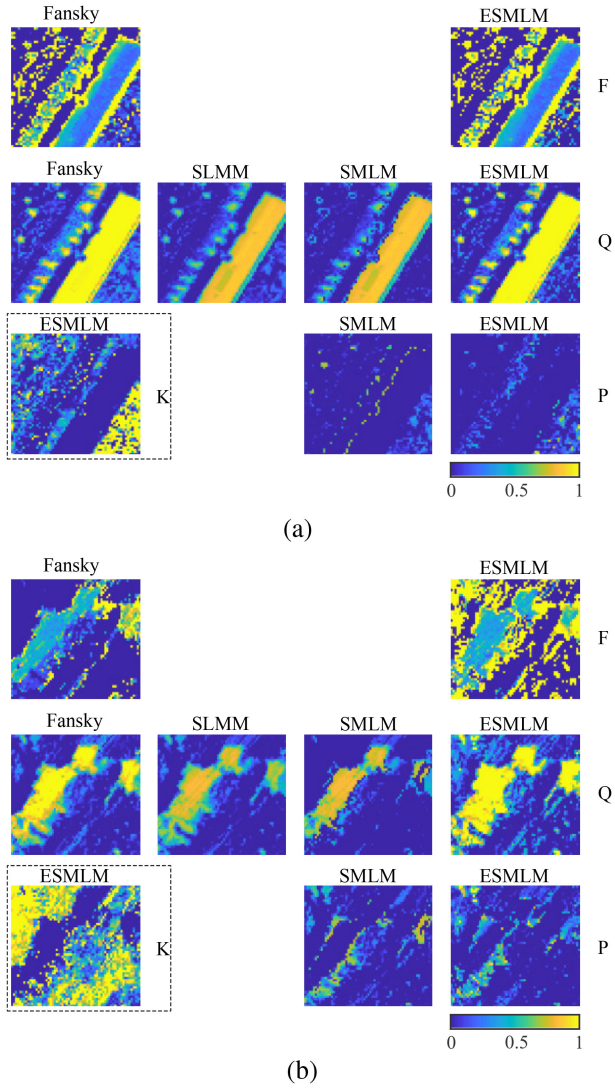

Fig. 11. Output parameter maps, from top to bottom: F (sky view factor), Q (spatial fraction of shadows), P (probability that a light ray undergoes additional interactions with endmembers), K (a strength factor of neighbor interactions, denoting the fraction of the scattered light from the neighborhood that is received by the pixel). Compared models, from left to right: Fansky, SLMM, SMLM, and ESMLM. (a) Subset 1. (b) Subset 2.

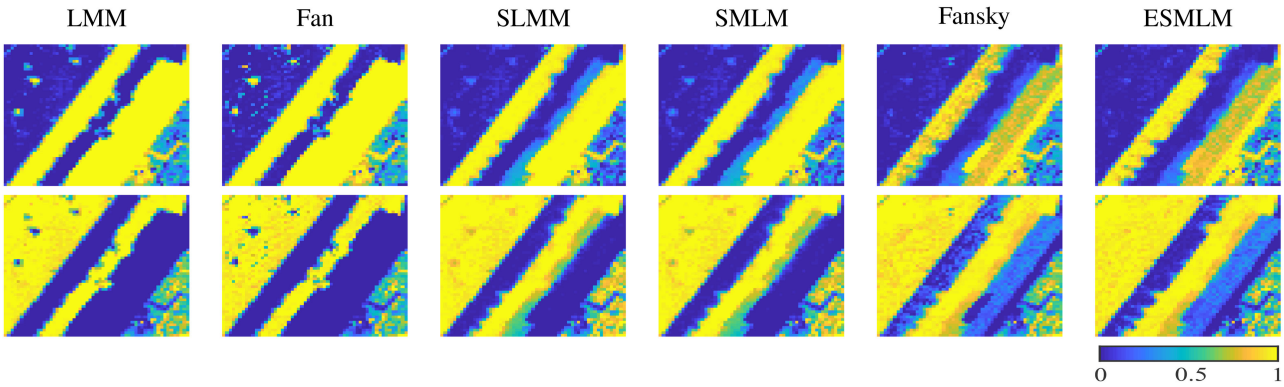

Fig. 12. Abundance maps of the real hyperspectral imagery without ground truth for subset 1. First row: Abundances of impervious materials; second row: Abundances of vegetation.

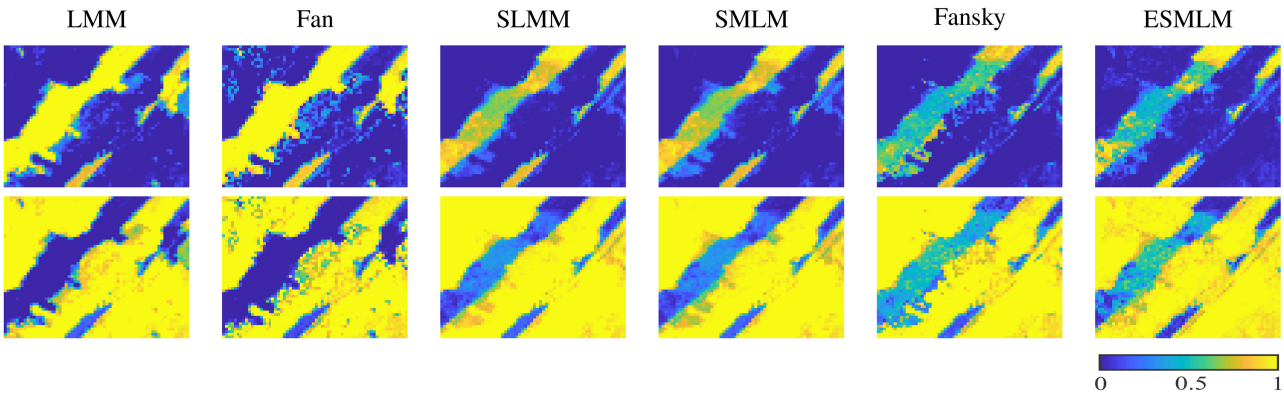

Fig. 13. Abundance maps of the real hyperspectral imagery without ground truth for subset 2. First row: Abundances of impervious materials; second row: Abundances of vegetation.

Finally, models accounting for skylight (ESMLM and Fansky) additionally output the topographic related parameter F, indicating the sky fraction that a ground pixel can "see." It is worth noting that F is only valid in (partly) shadowed pixels, as F is only involved in the skylight terms of the ESMLM and Fansky models. In this article, we set $F = 0$ in regions where $Q \leq 0.1$. Compared to the Fansky model, the ESMLM model is superior in estimating values of F in regions shadowed by vegetation. An example is shown in the upper-left corner of subset 2, where the Fansky model obtained zero F, and thus merely reconstructs shadows by scaling sunlit pixels. Instead, the ESMLM model can balance the values of F by contributions of P. In regions where Fansky produces $F = 0$, the reconstruction errors of the ESMLM model are consistently lower by a value of 0.03 on average.

D. Abundances

Besides parameters, the proposed method outputs abundances that present the material components at subpixel level. Since we do not have ground truth data for this real dataset, we evaluate abundances qualitatively in this section. Figs. 12 and 13 show the abundance maps for all comparing models in two subsets. For each subset, we present two aggregate abundance maps of impervious surfaces and vegetation, by grouping materials with similar spectra.

Abundances in fully sunlit pixels are comparable among all models while abundance maps show noticeably different patterns in (partly) shadowed pixels, depending on if and how the shadow and nonlinear effects are considered. In the LMM and Fan model, vegetation and impervious surface in the (partly) shadowed pixels are detected indiscriminately as impervious material. The reason is that the endmember library contains some impervious materials with low reflectances that are more similar to shadow spectra. Nevertheless, the LMM and Fan model show large RE values in (partly) shadowed pixels, indicating their unsatisfactory spectral representation in shadowed areas.

Results largely improve when considering shadow as a scaling effect, as is done by the SLMM and SMLM model. In the shadowed vegetation areas, SLMM and SMLM perform significantly better. Nevertheless, a small amount of impervious surface remains in shadowed vegetation areas because it is used to compensate for the inaccuracy of the shadow modeling.

The Fansky and ESMLM models, that consider the skylight information, improve the performance in shadowed vegetation regions while introducing more noise. Compared to the Fansky model, the ESMLM model presents better results on vegetation shadows, thanks to the advantageous modeling of the nonlinear effects.

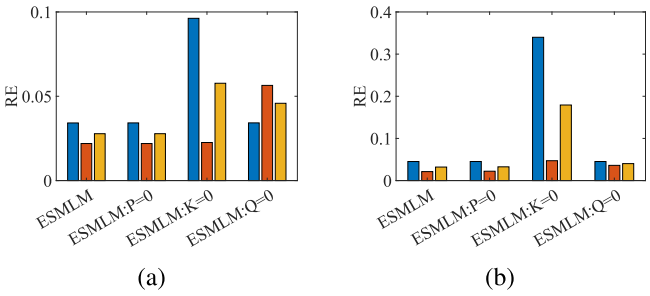

Fig. 14. Mean reconstruction error (RE) in the ablation study for subset 1 in (a) and subset 2 in (b). Blue: Fully sunlit pixels; Orange: (Partly) shadowed pixels; Yellow: The entire image. Fully sunlit and (partly) shadowed pixels are identified as $Q \leq 0.1$ and $Q > 0.1$, respectively, where Q values are computed using the full model.

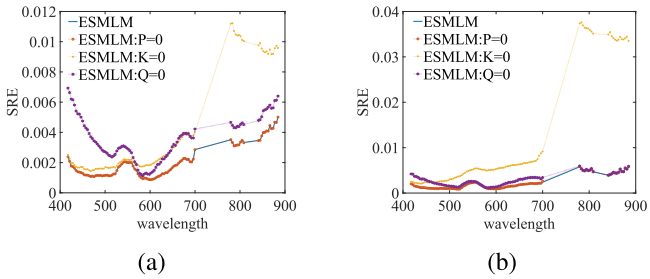

Fig. 15. Spectral reconstruction error (SRE) as a function of wavelength in the ablation study for subset 1 in (a) and subset 2 in (b).

Some open questions remain for the deeply shadowed pixels caused by vegetation. For example, abundances in the shadowed impervious regions are not as large as expected in subset 2. One reason can be that the incoming light from the global illumination first interacts with trees before reaching the road, mixing vegetation features in the backscattered signal in those regions. On the other hand, the LMM and Fan model estimate those regions as pure impervious materials, but it does not mean that they perform better, because they mainly confuse the shadowed pixels with impervious materials in the entire region.

E. Ablation Study

This section shows the results of an ablation study of the ESMLM model and analyzes the impact of the parameters P, Q, K by setting them to zero one at a time. Similar to the above experiments, we analyze the results in terms of reconstruction errors (see Figs. 14 and 15), shadow-removed reconstruction (see Figs. 16 and 17), and output parameter maps (see Fig. 18). We discuss the effect of each parameter in the following sections.

1) Role of Q: Q is the key parameter for modeling shadows. When $Q = 0$, the skylight-related terms become zero. Shadow removal cannot take place (see Fig. 16), and mean spectral errors would become undesirably large in Fig. 17. As the shadow-related terms are removed, RE largely increases in shadowed regions in subset 1. In addition, SRE goes up for all wavelengths, and a significant increase is observed in the spectral range of 400–550 nm. This change is caused by the lack of skylight terms, which largely impacts on shorter wavelengths. In subset 2, RE does not considerably increase in (partly) shadowed pixels [see Fig. 14(b)], whereas SRE increases at shorter wavelengths in the spectral range of 400–500 nm [see Fig. 15(b)]. The reason is that P replaces the role of Q to compensate for the reconstruction loss. In Fig. 18, it can be observed that the contribution of P increases. Despite a better reconstruction, this leads to an incorrect estimation of the parameters. This indicates that reconstruction errors cannot be the only measure to evaluate the performance of mixture models.

2) Role of P: P is relevant for the within-pixel nonlinear behavior. Removing P does not affect reconstruction errors (see Figs. 14 and 15), because Q and K compensate for the reconstruction loss. However, removing P impacts the estimation of other parameters [see Fig. 18(b)]. When $P = 0$, the neighbor effect term $(1-Q)(1-P)K\sum_{i=1}^{p} a_i \boldsymbol{e}_i \cdot \boldsymbol{e}_N$ becomes the only second-order reflection term in the model. Thus, the ablated model will estimate inaccurate values for Q, K, and F in vegetation shadows, where P is expected to have contributed. In addition, P plays an important role in removing shadow. When reconstructing the shadow-removed images, the sunlit regions should remain unchanged. However, we observed that the spectral distance using the l_2-norm between input and restored images in sunlit regions increased consistently by a value of 0.025 on average in sunlit regions when $P = 0$, compared to the full model.

3) Role of K: K is related to the between-pixel optical interactions that occur mainly in vegetated regions. When $K = 0$, the reconstruction errors largely increase in (partly) sunlit pixels (see Fig. 14). In addition, SRE increases at longer wavelengths, which is caused by not accounting for the multiple interactions of vegetation in the local neighborhood (see Fig. 15). At shorter wavelengths, SRE only slightly increases because the ablated model contains the key parameter Q for modeling shadows. The performance of shadow removal decreases when $K = 0$: Shadow-removed images lose textural information (see Fig. 16), and the mean spectral errors increase in subset 2, where vegetation dominates [see Fig. 17(f)].

F. Comparison Between Manual and Automatic Endmember Extraction Methods

In this section, we analyze the impact of endmember extraction methods on the result of the two subsets of the real hyperspectral image and compare the unmixing results using manually extracted endmembers with those using automatically extracted endmembers. Considering the shadow issue, we designed a simple but effective method to select fully sunlit pixels before automatic endmember extraction. First, we carefully set an empirical threshold (set to 0.08 in this article) and then select pixels with mean reflectance larger than 0.08 as candidate sunlit pixels. However, candidate sunlit pixels may include partly sunlit pixels located at shadow boundaries. Thus, we additionally apply a Canny edge detector [45] to remove all boundary pixels from sunlit pixels candidates. In addition, considering endmember variability, we apply the method in [46] to extract endmember bundles based on vertex component analysis [47]. Finally, we merge endmembers with similar reflectances and show the selected endmembers in Fig. 19(c).

We apply the automatically extracted endmembers to the two subsets of the real airborne hyperspectral imagery without

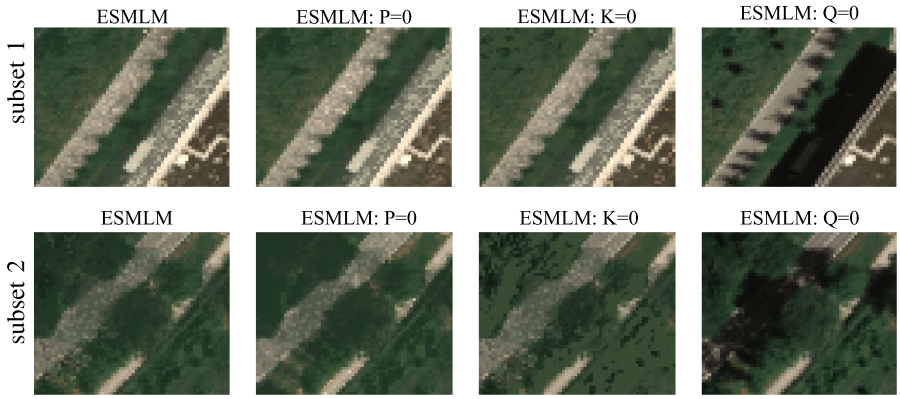

Fig. 16. Shadow-removed reconstructed images (true color composites) in the ablation study for subset 1 (first row) and subset 2 (second row).

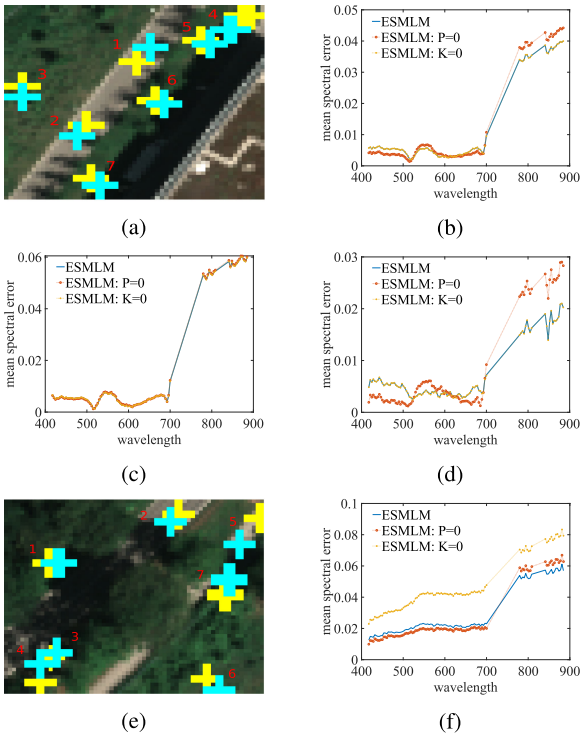

Fig. 17. Ablation study: Spectral comparison between shadowed pixels in shadow-removed images and their corresponding neighboring sunlit pixels, containing the same material. Subset 1: Locations of selected pairs of pixels in (a), spectral errors in all regions in (b), in regions shadowed by man-made objects in (c), and in regions shadowed by vegetation in (d). Subset 2: Location of selected pairs of pixels in (e), spectral errors in all regions (all regions are shadowed by vegetation) in (f). The ablated model with $Q = 0$ is not in the comparison, because it would exclude the shadow effect, causing undesirably large spectral errors.

ground truth. First, we compare the RE for subsets 1 and 2 in Fig. 19(f) and (g), respectively. Results depict that RE in (partly) shadowed pixels is comparable between automatic and manual endmember extraction methods. This is expected because (partly) shadowed pixels are excluded from the endmember extraction. In sunlit pixels, reconstruction errors decrease for all unmixing methods while their relative relationship remains, indicating that a better endmember library can be extracted using

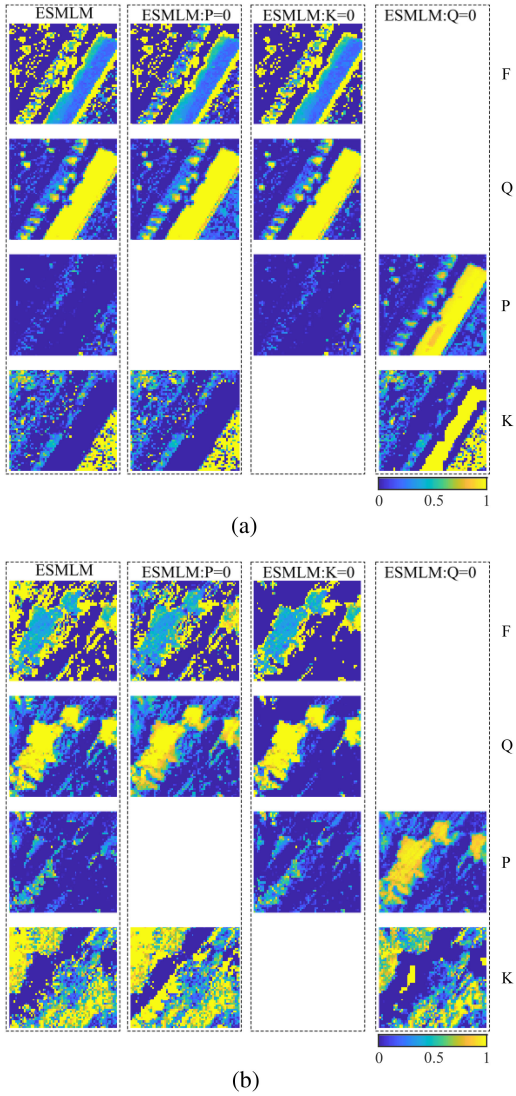

Fig. 18. Parameter maps in the ablation study. From top to bottom: F (the sky view factor), Q (the spatial fraction of shadow), P (the probability that a light ray undergoes additional interactions with endmembers), K (a strength factor of neighbor interactions, denoting the fraction of the scattered light from the neighborhood that is received by the pixel). From left to right: The ESMLM model, the ablated ESMLM models, with $P = 0$, $K = 0$, and $Q = 0$, respectively. (a) Subset 1. (b) Subset 2.

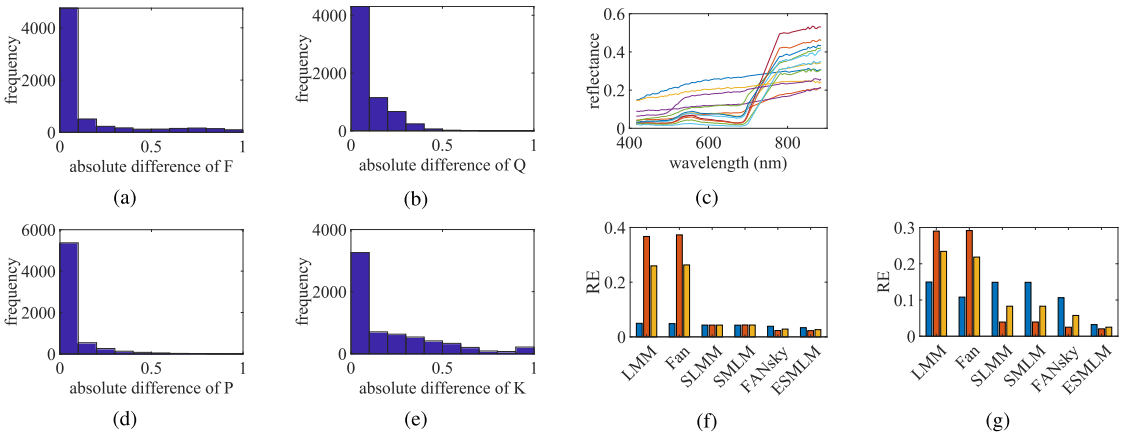

Fig. 19. Comparison between manual and automatic endmember extraction methods. Automatically extracted endmembers in (c), RE computed by unmixing methods with automatically extracted endmembers for subset 1 in (f) and subset 2 in (g), where blue, orange, and yellow colors represent fully sunlit pixels, (partly) shadowed pixels, and the entire image, respectively. Fully sunlit and (partly) shadowed pixels are identified as $Q \leq 0.1$ and $Q > 0.1$, respectively, where Q values are computed using the ESMLM model. Histogram of the absolute difference between manually and automatically extracted endmembers of parameter F in (a), Q in (b), P in (d), and K in (e).

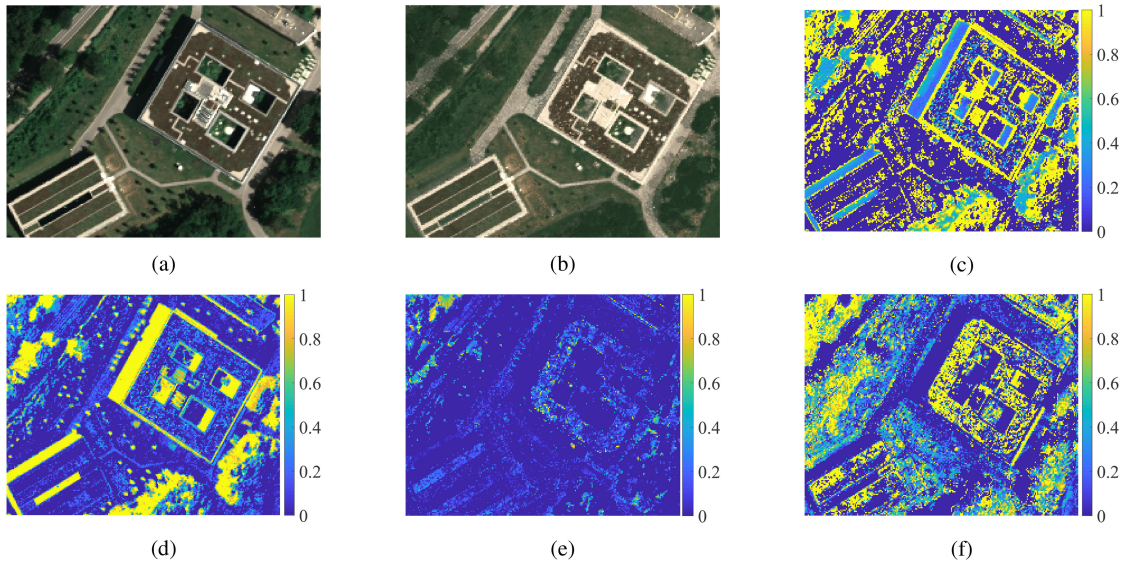

Fig. 20. Results on the entire test image. True composites of (a) original image and (b) shadow-removed image; parameter outputs F, Q, P, and K, are depicted in (c), (d), (e), and (f), respectively.

automatic endmember extraction. Moreover, we compare the output parameters (F, Q, P, and K) by the histogram of the parameter differences between the manually and automatically endmembers in Fig. 19(a), (b), (d), and (e). The differences between parameters estimated by two endmember libraries remain small, implying that results are not very sensitive to the endmember extraction method. We can conclude that manually extracted endmembers can be applied in our work.

G. Experimental Results and Discussion: The Entire Test Image

Finally, we applied the proposed model to the entire test image, resulting in mean reconstruction errors (RE) of 0.04 in fully sunlit pixels, 0.03 in (partly) shadowed pixels, and 0.03 in the entire image. The low variation of RE values between different categories of pixels indicates that the ESMLM model provides a robust pixel representation over various illumination conditions and local structures. In addition, the output parameters of the entire image [see Fig. 20(b) and (e)] follow similar patterns as in the subset images. By interpreting the parameters, one can easily detect the different illumination conditions and local structures illustrated in Fig. 1. Specifically, (partly) shadowed pixels contain high Q values while K mainly contributes in (partly) sunlit vegetated regions and becomes typically higher when vegetation has larger height variations, such as trees. Compared to K, P mainly plays a role in (partly) shadowed pixels occluded by vegetation. Besides indicating the local structures, output parameters also play an important role in reconstructing the shadow-removed image shown in Fig. 20(a).

IX. Conclusion

In this article, we proposed an ESMLM model for hyperspectral images based on radiative transfer theory, addressing shadow and nonlinear effects. The proposed model follows a graphical framework of mixture models, and sums up all possible radiation paths initiated by the illumination sources. Three illumination sources are considered: 1) direct, 2) diffuse, and 3) neighboring illuminations. The proposed model considers different shadow variants, i.e., fully shadowed pixels, partly shadowed, and spatially separable pixels, and partly shadowed but spatially inseparable pixels. Additionally, two types of nonlinear interactions for different illumination conditions have been modeled. Physical assumptions have been made to simplify the ESMLM model, leading to four physically interpretable parameters: P (the probability that a light ray undergoes additional interactions with endmembers), Q (the spatial fraction of shadow), F (the sky view factor), and K (a strength factor of neighbor interactions, denoting the fraction of the scattered light from the neighborhood that is received by the pixel). Given these physically interpretable parameters as output, the proposed model characterizes the local structures of the ground surface and allows us to reconstruct a shadow-removed image by simply "lighten up" the shadow-related terms.

We compared the proposed model with state-of-the-art mixture models on both synthetic dataset and real images with qualitative and quantitative measures. We first analyzed reconstruction and abundance errors on simulated data with and without additional noise. After that, we simulated (partly) shadowed pixels in a real hyperspectral imagery with known abundance ground truth, and evaluated the performance of different mixture models. Furthermore, we analyzed the unmixing models in airborne hyperspectral images with real shadowed pixels. Specifically, we discussed the reconstruction errors in spatial and spectral domains, and we compared shadow-removed images and model output parameters. Experimental results demonstrate that the proposed model performs consistently better in different ground scenarios with various illumination conditions. Moreover, we conducted an ablation study of the ESMLM model, in which we studied the role and significance of each parameter separately. Experimental results demonstrate that the full model performs better than the ablated models.

Several open problems remain. First, when including the skylight information, the shadow-removed images contain higher levels of noise, caused either by the low signal-to-noise ratio or by strong nonlinear effects that take place in (partly) shadowed pixels. In addition, spectral errors of the proposed model, even though lower than in other models, remain large in some shadowed regions. Future work concerns including spatial information in the mixture model to promote spatial correlations among pixels.

References

[1] P. Ghamisi *et al.*, "Advances in hyperspectral image and signal processing: A comprehensive overview of the state of the art," *IEEE Geosci. Remote Sens. Mag.*, vol. 5, no. 4, pp. 37–78, Dec. 2017.

[2] M. J. Khan, H. S. Khan, A. Yousaf, K. Khurshid, and A. Abbas, "Modern trends in hyperspectral image analysis: A review," *IEEE Access*, vol. 6, pp. 14118–14129, 2018.

[3] D. Landgrebe, "Hyperspectral image data analysis," *IEEE Signal Process. Mag.*, vol. 19, no. 1, pp. 17–28, Jan. 2002.

[4] S. Chandrasekhar, *Radiative Transfer (Ser. Dover Books on Physics)*. New York, NY, USA: Dover, 2013. [Online]. Available: https://books.google.de/books?id=1YHCAgAAQBAJ

[5] J. Lenoble, *Atmospheric Radiative Transfer (Ser. Stud. in Geophysical Opt. and Remote Sens.)*. Hampton, VA, USA: Deepak Pub., 1993. [Online]. Available: https://books.google.de/books?id=WDBRAAAAMAAJ

[6] R. Richter, D. Schläpfer, and A. Müller, "An automatic atmospheric correction algorithm for visible/NIR imagery," *Int. J. Remote Sens.*, vol. 27, no. 10, pp. 2077–2085, 2006.

[7] R. Richter and D. Schläpfer, "Geo-atmospheric processing of airborne imaging spectrometry data. Part 2: Atmospheric/topographic correction," *Int. J. Remote Sens.*, vol. 23, no. 13, pp. 2631–2649, 2002.

[8] J. M. Bioucas-Dias *et al.*, "Hyperspectral unmixing overview: Geometrical, statistical, and sparse regression-based approaches," *IEEE J. Sel. Topics Appl. Earth Observ. Remote Sens.*, vol. 5, no. 2, pp. 354–379, Apr. 2012.

[9] R. Heylen, M. Parente, and P. Gader, "A review of nonlinear hyperspectral unmixing methods," *IEEE J. Sel. Topics Appl. Earth Observ. Remote Sens.*, vol. 7, no. 6, pp. 1844–1868, Jun. 2014.

[10] N. Dobigeon, J.-Y. Tourneret, C. Richard, J. C. M. Bermudez, S. McLaughlin, and A. O. Hero, "Nonlinear unmixing of hyperspectral images: Models and algorithms," *IEEE Signal Process. Mag.*, vol. 31, no. 1, pp. 82–94, Jan. 2014.

[11] C. C. Borel, S. A. Gerstl, and B. J. Powers, "The radiosity method in optical remote sensing of structured 3-D surfaces," *Remote Sens. Environ.*, vol. 36, no. 1, pp. 13–44, 1991. [Online]. Available: https://www.sciencedirect.com/science/article/pii/0034425791900285

[12] C. C. Borel and S. A. Gerstl, "Nonlinear spectral mixing models for vegetative and soil surfaces," *Remote Sens. Environ.*, vol. 47, no. 3, pp. 403–416, 1994. [Online]. Available: https://www.sciencedirect.com/science/article/pii/0034425794901074

[13] N. Keshava and J. F. Mustard, "Spectral unmixing," *IEEE Signal Process. Mag.*, vol. 19, no. 1, pp. 44–57, Jan. 2002.

[14] M.-D. Iordache, J. M. Bioucas-Dias, and A. Plaza, "Sparse unmixing of hyperspectral data," *IEEE Trans. Geosci. Remote Sens.*, vol. 49, no. 6, pp. 2014–2039, Jun. 2011.

[15] F. Zhu, Y. Wang, B. Fan, S. Xiang, G. Meng, and C. Pan, "Spectral unmixing via data-guided sparsity," *IEEE Trans. Image Process.*, vol. 23, no. 12, pp. 5412–5427, Dec. 2014.

[16] J. Bieniarz, E. Aguilera, X. X. Zhu, R. Müller, and P. Reinartz, "Joint sparsity model for multilook hyperspectral image unmixing," *IEEE Geosci. Remote Sens. Lett.*, vol. 12, no. 4, pp. 696–700, Apr. 2015.

[17] J. Liu, J. Zhang, Y. Gao, C. Zhang, and Z. Li, "Enhancing spectral unmixing by local neighborhood weights," *IEEE J. Sel. Topics Appl. Earth Observ. Remote Sens.*, vol. 5, no. 5, pp. 1545–1552, Oct. 2012.

[18] M.-D. Iordache, J. M. Bioucas-Dias, and A. Plaza, "Total variation spatial regularization for sparse hyperspectral unmixing," *IEEE Trans. Geosci. Remote Sens.*, vol. 50, no. 11, pp. 4484–4502, Nov. 2012.

[19] Z. Mitraka, F. Del Frate, and F. Carbone, "Nonlinear spectral unmixing of landsat imagery for urban surface cover mapping," *IEEE J. Sel. Topics Appl. Earth Observ. Remote Sens.*, vol. 9, no. 7, pp. 3340–3350, Jul. 2016.

[20] B. Hapke, "Bidirectional reflectance spectroscopy: 1. Theory," *J. Geophys. Res.: Solid Earth*, vol. 86, no. B4, pp. 3039–3054, 1981.

[21] J. M. Nascimento and J. M. Bioucas-Dias, "Nonlinear mixture model for hyperspectral unmixing," *Proc. SPIE*, vol. 7477, 2009, Art. no. 74770I.

[22] W. Fan, B. Hu, J. Miller, and M. Li, "Comparative study between a new nonlinear model and common linear model for analysing laboratory simulated-forest hyperspectral data," *Int. J. Remote Sens.*, vol. 30, no. 11, pp. 2951–2962, 2009.

[23] Y. Altmann, A. Halimi, N. Dobigeon, and J.-Y. Tourneret, "Supervised nonlinear spectral unmixing using a polynomial post nonlinear model for hyperspectral imagery," in *Proc. IEEE Int. Conf. Acoust., Speech, Signal Process.*, 2011, pp. 1009–1012.

[24] A. Halimi, Y. Altmann, N. Dobigeon, and J.-Y. Tourneret, "Nonlinear unmixing of hyperspectral images using a generalized bilinear model," *IEEE Trans. Geosci. Remote Sens.*, vol. 49, no. 11, pp. 4153–4162, Nov. 2011.

[25] I. Meganem, P. Déliot, X. Briottet, Y. Deville, and S. Hosseini, "Linear-quadratic mixing model for reflectances in urban environments," *IEEE Trans. Geosci. Remote Sens.*, vol. 52, no. 1, pp. 544–558, Jan. 2014.
[26] A. Marinoni, A. Plaza, and P. Gamba, "Harmonic mixture modeling for efficient nonlinear hyperspectral unmixing," *IEEE J. Sel. Topics Appl. Earth Observ. Remote Sens.*, vol. 9, no. 9, pp. 4247–4256, Sep. 2016.
[27] A. Marinoni and P. Gamba, "A novel approach for efficient *p*-linear hyperspectral unmixing," *IEEE J. Sel. Topics Signal Process.*, vol. 9, no. 6, pp. 1156–1168, Sep. 2015.
[28] R. Heylen and P. Scheunders, "A multilinear mixing model for nonlinear spectral unmixing," *IEEE Trans. Geosci. Remote Sens.*, vol. 54, no. 1, pp. 240–251, Jan. 2015.
[29] R. Heylen, V. Andrejchenko, Z. Zahiri, M. Parente, and P. Scheunders, "Nonlinear hyperspectral unmixing with graphical models," *IEEE Trans. Geosci. Remote Sens.*, vol. 57, no. 7, pp. 4844–4856, Jul. 2019.
[30] S. M. Adler-Golden, M. W. Matthew, G. P. Anderson, G. W. Felde, and J. A. Gardner, "Algorithm for de-shadowing spectral imagery," *Proc. SPIE*, 2002, vol. 4816, pp. 203–210.
[31] A. Plaza, P. Martínez, R. Pérez, and J. Plaza, "A quantitative and comparative analysis of endmember extraction algorithms from hyperspectral data," *IEEE Trans. Geosci. Remote Sens.*, vol. 42, no. 3, pp. 650–663, Mar. 2004.
[32] F. Kruse *et al.*, "The spectral image processing system (SIPS)—Interactive visualization and analysis of imaging spectrometer data," *Remote Sens. Environ.*, vol. 44, no. 2, pp. 145–163, 1993. [Online]. Available: https://www.sciencedirect.com/science/article/pii/003442579390013N
[33] J. Yang, Y. He, and J. Caspersen, "Fully constrained linear spectral unmixing based global shadow compensation for high resolution satellite imagery of urban areas," *Int. J. Appl. Earth Observ. Geoinf.*, vol. 38, pp. 88–98, 2015.
[34] F. Omruuzun, D. O. Baskurt, H. Daglayan, and Y. Y. Cetin, "Shadow removal from VNIR hyperspectral remote sensing imagery with endmember signature analysis," *Proc. SPIE*, 2015, vol. 9482, Art. no. 94821F.
[35] M. Zhao, J. Chen, and S. Rahardja, "Hyperspectral shadow removal via nonlinear unmixing," *IEEE Geosci. Remote Sens. Lett.*, vol. 18, no. 5, pp. 881–885, May 2021.
[36] F. Yamazaki, W. Liu, and M. Takasaki, "Characteristics of shadow and removal of its effects for remote sensing imagery," in *Proc. IEEE Int. Geosci. Remote Sens. Symp.*, 2009, vol. 4, 2009, pp. IV-426–IV-429.
[37] J. R. Schott, *Remote Sensing: The Image Chain Approach*. London, U.K.: Oxford Univ. Press, 2007.
[38] T. Uezato, N. Yokoya, and W. He, "Illumination invariant hyperspectral image unmixing based on a digital surface model," *IEEE Trans. Image Process.*, vol. 29, no. 1, pp. 3652–3664, Jan. 2020.
[39] G. Zhang, D. Cerra, and R. Müller, "Shadow detection and restoration for hyperspectral images based on nonlinear spectral unmixing," *Remote Sens.*, vol. 12, no. 23, 2020, Art. no. 3985.
[40] M. K. Svensson, "Sky view factor analysis-implications for urban air temperature differences," *Meteorol. Appl.*, vol. 11, no. 3, pp. 201–211, 2004.
[41] D. Kaskaoutis, H. Kambezidis, and Z. Toth, "Investigation about the dependence of spectral diffuse-to-direct-beam irradiance ratio on atmospheric turbidity and solar zenith angle," *Theor. Appl. Climatol.*, vol. 89, no. 3, pp. 245–256, 2007.
[42] R. E. Bird and C. Riordan, "Simple solar spectral model for direct and diffuse irradiance on horizontal and tilted planes at the Earth's surface for cloudless atmospheres," *J. Appl. Meteorol. Climatol.*, vol. 25, no. 1, pp. 87–97, 1986.
[43] D. Cerra *et al.*, "DLR HySU—A benchmark dataset for spectral unmixing," *Remote Sens.*, vol. 13, no. 13, 2021, Art. no. 2559.
[44] C. H. Köhler, "Airborne imaging spectrometer hyspex," *J. Large-Scale Res. Facilities*, vol. 2, no. A93, pp. 1–6, 2016.
[45] J. Canny, "A computational approach to edge detection," *IEEE Trans. Pattern Anal. Mach. Intell.*, vol. PAMI-8, no. 6, pp. 679–698, Nov. 1986.
[46] B. Somers, M. Zortea, A. Plaza, and G. P. Asner, "Automated extraction of image-based endmember bundles for improved spectral unmixing," *IEEE J. Sel. Topics Appl. Earth Observ. Remote Sens.*, vol. 5, no. 2, pp. 396–408, Apr. 2012.
[47] J. M. Nascimento and J. M. Dias, "Vertex component analysis: A fast algorithm to unmix hyperspectral data," *IEEE Trans. Geosci. Remote Sens.*, vol. 43, no. 4, pp. 898–910, Apr. 2005.

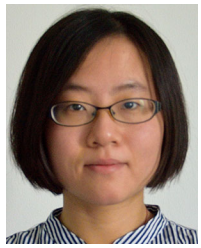

Guichen Zhang received the B.Sc. degree in remote sensing science and technology from Wuhan University, Wuhan, China, in 2014, the M.Sc. degree in earth-oriented space science and technology from the Technical University of Munich, Munich, Germany, in 2018, and the M.Sc. degree in photogrammetry and remote sensing from Wuhan University, in 2018. Since 2018, she has been working toward the Ph.D. degree with the German Aerospace Center, Weßling, Germany.

In 2021, she was a Visiting Scientist with the Physics Department, University of Antwerp. Her research interests include image processing, hyperspectral image analysis, data fusion, and machine learning in the application of remote sensing.

Paul Scheunders (Senior Member, IEEE) received the B.S. and Ph.D. degrees in physics, with work in the field of statistical mechanics, from the University of Antwerp, Antwerp, Belgium, in 1983 and 1990, respectively.

In 1991, he became a Research Associate with Vision Lab, Department of Physics, University of Antwerp, where he is currently a Full Professor. He has authored or coauthored more than 200 papers in international journals and proceedings in the field of image processing, pattern recognition, and remote sensing. His current research interest includes remote sensing and hyperspectral image processing.

Dr. Scheunders is an Associate Editor for the IEEE TRANSACTIONS ON GEOSCIENCE AND REMOTE SENSINGand has served as a Program Committee Member in numerous international conferences. He is a Senior Member of the IEEE Geoscience and Remote Sensing Society.

Daniele Cerra (Member, IEEE) received the M.Sc. degree in computer engineering from Roma Tre University, Rome, Italy, in 2005, the M.Sc. degree in GIS from Salamanca University, Salamanca, Spain, in 2006, and the Ph.D. degree (high Hons.) in image and signal processing from Télécom Paristech University, Paris, France, in 2010.

He has been with the Department of Photogrammetry and Image Analysis, German Aerospace Center (DLR), Oberpfaffenhofen, Germany. He has been teaching digital image processing and hyperspectral remote sensing since 2012 as a Visiting Lecturer or Professor in several universities (Spain, Germany, Italy, and Iran), and since 2014 as a trainer with the European Space Agency.

He authored or coauthored more than 100 publications in peer-reviewed journals, books, or international conferences. His research interests include hyperspectral imaging, data fusion, and algorithmic information theory.

Dr. Cerra won a total of five prizes (three as first author) in the IEEE GRSS Data Fusion Contests in the years 2013–2020. He won the DLR Science Slam contest in 2013 and coauthored the best paper in the IEEE Whispers 2019 conference.

Rupert Müller received the Dipl.-Phys. degree in physics from the Ludwig Maximilians University of Munich, Munich, Germany, in 1984.

He is currently a Team Leader of the "Hyperspectral Remote Sensing and Traffic Monitoring" group, Remote Sensing Technology Institute, German Aerospace Center (DLR), Wessling, Germany, and also a Project Manager of the Ground Segment of MUSES (Multiuser System for Earth Sensing) with the hyperspectral instrument DESIS (DLR Earth Sensing Imaging Spectrometer) installed on the International Space Station. His main research interests include photogrammetric evaluation of optical data from air- and spaceborne sensors, digital image processing, machine learning, and hyperspectral imaging.